ISTANBUL TECHNICAL UNIVERSITY ★ GRADUATE SCHOOL OF SCIENCE ENGINEERING AND TECHNOLOGY

INTEGRATION OF REMOTE SENSING AND GIS FOR MONITORING THE AREAS AFFECTED BY FOREST FIRES: A CASE STUDY OF IZMIR, MENDERES

M.Sc. THESIS

Emre ÇOLAK

Department of Geomatics Engineering

Geomatics Engineering Programme

DECEMBER 2018

**ISTANBUL TECHNICAL UNIVERSITY ★ GRADUATE SCHOOL OF SCIENCE
ENGINEERING AND TECHNOLOGY**

**INTEGRATION OF REMOTE SENSING AND GIS FOR MONITORING THE
AREAS AFFECTED BY FOREST FIRES: A CASE STUDY OF IZMIR,
MENDERES**

M.Sc. THESIS

Emre ÇOLAK
(501171617)

Department of Geomatics Engineering

Geomatics Engineering Programme

Thesis Advisor: Prof. Dr. A. Filiz SUNAR

DECEMBER 2018

ISTANBUL TEKNİK ÜNİVERSİTESİ ★ FEN BİLİMLERİ ENSTİTÜSÜ

ORMAN YANGIN ALANLARININ UZAKTAN ALGILAMA VE CBS ENTEGRASYONU İLE İZLENMESI: İZMİR, MENDERES ÖRNEĞİ

YÜKSEK LİSANS TEZİ

Emre ÇOLAK
(501171617)

Geomatik Mühendisliği Anabilim Dalı

Geomatik Mühendisliği Programı

Tez Danışmanı: Prof. Dr. A. Filiz SUNAR

ARALIK 2018

Emre Çolak, a M.Sc. student of İTU Graduate School of Science Engineering and Technology student ID 501171617, successfully defended the thesis/dissertation entitled "INTEGRATION OF REMOTE SENSING AND GIS FOR MONITORING THE AREAS AFFECTED BY FOREST FIRES: A CASE STUDY OF IZMIR, MENDERES", which he prepared after fulfilling the requirements specified in the associated legislations, before the jury whose signatures are below.

Thesis Advisor :   **Prof. Dr. A. Filiz SUNAR**   ....
İstanbul Technical University

Jury Members :   **Prof. Dr. Nebiye Musaoğlu**   ....
Istanbul Technical University

Prof. Dr. Zafer Aslan   ....
Istanbul Aydın University

Date of Submission : 16.11.2018
Date of Defense   : 21.12.2018

v

To my family,

FOREWORD

First of all, I would like to tender my gratefulness to my advisor Professor Filiz Sunar for her ongoing supervision, guidance, and inspiration throughout the course of my research. Professor Filiz Sunar is a wonderful scientist with great abilities, it was an honor for me to have the opportunity to work with her.

I would to thank my mother Işık Çolak, my father Ali Çolak, and my sisters Burcu Çolak Ayık and Cansu Çolak Öz for their unflagging support and encouragement during my education. I would also like to thank Selda Işkın for her continous support, advice and encouragement that lighted up my way. I will forever indebted to my family. I would also like to offer my thank to my friends.

Lastly, I wish to thank Izmir Forestry Chief Directorate for GIS data supply and support.

<table>
<tr><td>November 2018</td><td style="text-align:right">Emre ÇOLAK
Geomatics Engineer</td></tr>
</table>

TABLE OF CONTENTS

ABBREVIATIONS

GIS	**:** Geographic Information Systems	
NASA	**:** National Aeronautics and Space Administration	
USGS	**:** United States Geological Survey	
ESA	**:** European Space Agency	
OLI	**:** Operational Land Imager	
TIRS	**:** Thermal Infrared Sensor	
MSI	**:** Multi Spectral Instrument	
ISODATA	**:** Iterative Self-Organizing Data Analysis Technique	
LST	**:** Land Surface Temperature	

SYMBOLS

c   **:** Speed of light

E   **:** Energy

h   **:** Planck constant

f   **:** Frequency

λ   **:** Wavelength

σ   **:** Stefan-Boltzman constant

k   **:** Boltzman constant

A   **:** Wien's displacement constant

T   **:** Temperature

M   **:** Spectral exitance

L$_\lambda$ **:** Spectral radiance

LIST OF TABLES

LIST OF FIGURES

INTEGRATION OF REMOTE SENSING AND GIS FOR MONITORING THE AREAS AFFECTED BY FOREST FIRES: A CASE STUDY OF IZMIR, MENDERES

SUMMARY

In this thesis, a forest fire occured in Menderes, Izmir on July 1, 2017 was analyzed by a integration of pre-fire and post-fire Sentinel 2 and Landsat 8 satellite images with a Geographical Information System (GIS) data obtained from a field study conducted by Izmir Forestry Chief Directorate.

For this purpose, remote sensing techniques such as spectral burn indexes (Burn Area Index (BAI), Normalized Burn Ratio (NBR) and Normalized Burn Ratio – Thermal (NBRT) and Mid-Infrared Burn Index (MIRBI)), burn severity (dNBR), land surface temperature determination, and classification, together with GIS analysis were applied to the pre-fire and post-fire satellite images to monitor, analyse, and map the effects of the forest fire occured in Menderes region.

The spectral burn idexes BAI, NBR, NBRT, and MIRBI were applied on the post-fire Landsat 8 satellite image to extract and analyse the burned forest area. The NBR and NBRT indexes were very succesful to seperate the burned forest area from unburned areas. However, it is monitored that the BAI and MIRBI indexes could not completely distinguish the burned forest area from unburned areas, and they are mixed with other land covers especially with water bodies.

The burn severity was generated from post-fire (16.07.2017) and pre-fire (30.06.2017) Landsat 8 images by the use of dNBR index which computes the difference of NBR data sets. The same process was applied on 03.07.2018 dated post-fire Landsat 8 image to monitor the vegetation survival and mortality after one year later of the fire as the dNBR index shows also the vegetation regrowth. As a result, no vegetation regrowth was observed in the forest area after one year, and the effects of the fire are still the same.

Land Surface Temperature (LST) was also estimated by the use of land surface temperature method to monitor the changes of LST (dLST) in the Menderes region from pre-fire (30.06.2017) and post-fire (16.07.2017) Landsat 8 images. As a result, it was observed that the LST of the burned forest area was increased from 1 to 11 C° compared to unburned areas. The reason for the LST increase in burned areas is thought as the decrease of albedo (lower albedo leads to absorption of more solar energy at surface).

A correlation analysis was applied on dLST and burn severity (dNBR) to observe the possible relationship on these two variables. Eventually, a high correlation (R = 0.8138) was observed between the dNBR and the dLST. In addition, correlation analysis of dBAI, dMIRBI and dNBRT, obtained from other spectral burn indexes, with the dLST data were performed; moreover, dMIRBI and dNBRT indexes were found to be related to dLST (R = -0.7520 and R = 0.8567, repectively). However, the correlation coefficient between dBAI and dLST was found as zero (R = 0).

ISODATA classification method was performed on post-fire Sentinel 2 (10 m and 20 m spatial resolution) and Landsat 8 (30 m spatial resolution) satellite images. After applying the ISODATA classification algorithm as unsupervised classification method on three mentioned images, the area extent of burned areas was found as 972,9 ha, 938,61 ha, and 926,91 ha for the Sentinel (10 m), Sentinel (20 m), and Landsat 8 (30 m) satellite images respectively (the areal extent of burned area was measured as 986 ha by the Izmir Forestry Chief Directorate after a field work). As supervised classification method Maximum Likelihood and Support Vector Machine classification algorithms were applied on post-fire satellite images. As a result, burned forest areas were detemined as 962.37 ha, 963,36 ha, and 911,34 ha for 10 m Sentinel, 20 m Sentinel, and 30 m Landsat 8 satellite images respectively, and the overall accuracies were computed as 96.43 %, 82.22 %, and 80.30 % for Sentinel (10 m), Sentinel (20 m), and Landsat (30 m) respectively. The areal extent were calculated from Support Vector Machine method was found as 991,35 ha, 994,65 ha, and 997,11 ha for 10 m Sentinel, 20 m Sentinel, and 30 m Landsat 8 satellite images respectively. Furthermore, the overall accuracies of the classification results were found as 99.56 %, 97.86 %, and 97.52 % for 10 m Sentinel, 20 m Sentinel, and 30 m Landsat 8 images respectively.

Consequently, a GIS data was integrated with the remote sensing images; moreover, a slope and canopy density map were generated, and their relationship with the burned forest area and burn severity were determined. It was observed that slope from 29 to 41%, and the canopy density between 71 and 100 % were effecting the burned forest area. Moreover, according to the results slope from 29 to 41%, and the canopy density between 71 and 100 % were mostly determined as low burn severity.

In this study, it is shown that remote sensing and GIS techniques can be successfully used to monitor the areas affected by forest fires.

ORMAN YANGIN ALANLARININ UZAKTAN ALGILAMA VE CBS ENTEGRASYONU İLE İZLENMESİ: İZMİR, MENDERES ÖRNEĞİ

ÖZET

21. yüzyılda insanlık büyük bilimsel keşifler yaptı. Dünyayı fiziksel olarak anlama ve analiz etme konusunda ortaya çıkan bu temel keşiflere paralel olarak teknolojiyi geliştirmek mümkün oldu.

Sanayi devriminin bir sonucu olarak, artan insan nüfusu ve doğal kaynaklara olan talep, dünya üzerinde fiziksel olarak büyük bir değişime yol açmaktadır. Doğal kaynak tüketiminin yoğun bir şekilde artması ve doğanın insan tarafından tahrip edilmesi, küresel ısınma gibi feci sonuçlara neden olmaktadır. Ayrıca deprem, tsunami ve orman yangınları gibi doğal afetler sebebiyle bilgi ve teknolojiyi kullanarak çevreyi gözlemlemek ve kavramak elzem bir hâl almıştır. 2. Dünya Savaşı ile gelişen uzaktan algılama teknolojisi bu çevresel sorunları geçmişten günümüze yaratmış olduğu veri deposuyla daha da yakından takip etmemize ayrıca gezegende meydana gelebilecek tüm felaketleri tahmin ve analiz etmemize yardımcı olacaktır.

Uzaktan Algılama, özellikle 2. Dünya Savaşı'ndan sonra geliştirilen havacılık ve uzay teknolojileri ile en önemli bilimsel ve teknik alanlardan biri haline gelmiştir. Uzaktan algılama tekniklerinin temel amacı, insansız hava araçlarının (İHA), uçakların ve uyduların kullanımıyla dünya yüzeyindeki karaların, okyanusların ve buz tabakalarının gözlemlenmesidir. Uzaktan algılama görüntüleri, ormancılık, tarım, jeoloji, meteoroloji gibi bir topografik, oşinografik ve atmosferik uygulamalarda yaygın olarak kullanılmaktadır. Bu görüntüler, dünya yüzeyinin zaman içindeki değişimlerini izlemeyi mümkün kılmakta ayrıca bu değişimlerin ölçülmesini sağladığından oldukça önemlidirler.

Uzaktan algılamayı tanımlamak gerekirse, bir nesneden fiziksel temas olmaksızın elektromanyetik enerji ile bilgi toplanmasını ve kaydedilmesini sağlayan bilim ve teknolojidir. Uzaktan algılamanın tanımı geniş anlamda çok sayıda teknoloji içermesine rağmen, tüm uzaktan algılama teknolojileri belli temel kavramlara dayanmakta ve aynı temel bileşenleri içermektedir. Sistemdeki ana bileşenler hedef, enerji kaynağı, iletim yolu ve bir algılayıcıdır.

Coğrafi Bilgi Sistemi (CBS) ise coğrafi amaçlar için geniş ölçekli görevleri uygulamak amacıyla özel olarak tasarlanmış bir yazılım paketi olarak tanımlanmaktadır. CBS sisteminin temel görevleri verinin girişi, depolanması, işlenmesi, analiz edilmesi, yönetilmesi ve görüntülenmesi şeklindedir.

Coğrafi Bilgi Sistemi'nin 1960'ların ortalarında ortaya çıkmasıyla birlikte uzaktan algılama verilerinin ve CBS verileriyle entegrasyonu, çevrenin modellenmesi, analiz edilmesi ve haritalanması için kullanılmıştır. Dolayısıyla, uzaktan algılama verilerinde CBS'nin kullanımı kartografik ve tematik bilgiyi geliştirmiştir. CBS ile uzaktan algılama entegrasyonu görüntü işleme tekniklerinin de gelişmini sağlamıştır.

Orman yangını analizi, uzaktan algılama ve CBS entegrasyonunun önemli uygulamalarından biridir. Bir yangının başlangıcını ve yayılmasını etkileyen parametrelerin çeşitliliği nedeniyle, orman yangınının bu verilerin entegrasyonu ile analizini zorunlu kılmaktadır. Uzaktan algılama ve CBS entegrasyonunun yerel,

bölgesel ve küresel ölçekte orman yangınlarını izleme ve haritalamada en yararlı ve etkili yol olduğu söylenebilir.

Bu tez çalışmasında, 1 Temmuz 2017 tarihinde İzmir Orman Genel Müdürlüğü sınırları içerisinde bulunan Menderes ilçesinde meydana gelen bir orman yangını, yangın öncesi ve sonrası elde edilen Sentinel 2 ve Landsat 8 uydu görüntülerinin, İzmir Orman Genel Müdürlüğü tarafından gerçekleştirilen bir arazi çalışmasından elde edilen CBS verisi entegrasyonu ile analiz edilmiştir.

Gerçekleşen bu yangının sonuçlarını gözlemlemek, analiz etmek ve haritalamak için yangın öncesi ve sonrası elde edilen Sentinel 2 ve Landsat 8 uydu görüntülerine spektral yanma indeksleri (Yanan Alan Indeksi (Burn Area Index - BAI), Orta Kızılötesi Yanma İndeksi (Mid Infrared Burn Index - MIRBI), Normalize Edilmiş Yanma Şiddeti (Normalized Burn Ratio - NBR) ve Normalize Edilmiş Isıl Yanma Şiddeti (Normalized Burn Ratio Thermal - NBRT), sınıflandırma (ISODATA, Maksimum Benzerlik ve Destek Vektör Makineleri), yanma şiddetini (dNBR) ve yeryüzü yüzey sıcaklığını belirleme ayrıca CBS verisiyle entegrasyon gibi farklı görüntü işleme teknikleri uygulanmıştır.

Yanmış orman alanını belirlemek ve analiz etmek için yangından sonra algılanmış olan Landsat 8 uydu görüntüsüne BAI, NBR, NBRT ve MIRBI spektral yanma indeksleri uygulanmıştır. Yanmış orman bölgesini yanmamış bölgelerden ayırt etmede NBR ve NBRT indekslerinin oldukça başarılı oldukları gözlemlenmiştir. Ancak, BAI ve MIRBI indekslerinin yanmış orman alanlarını yanmamış alanlardan tamamen ayırt edemedikleri ve özellikle su alanları ile karıştırdığı görülmüştür.

Yanma şiddeti, yangın sonrası (16.07.2017) ve yangın öncesi (30.06.2017) Landsat 8 görüntülerinden, NBR veri kümelerinin farkını hesaplayan dNBR indeksi kullanılarak üretilmiştir. Aynı işlem yangından tam bir yıl sonra algılanmış olan 03.07.2018 tarihli Landsat 8 görüntüsüne de uygulanarak bitki örtüsünde bir iyileşme olup olmadığı gözlemlenmeye çalışılmış fakat aradan bir yıl geçmesine rağmen yangının sonuçlarının herhangi bir şekilde değişmediği ortaya konmuştur.

Yeryüzü yüzey sıcaklığını (LST) ve değişimini (dLST) belirlemek için yangın öncesi (30.06.2017) ve sonrası (16.07.2017) Landsat 8 görüntülerine yeryüzü yüzey sıcaklığı metodu uygulanmıştır. Elde edilen bilgiler ışığında yangın sonrası yanmış orman alanının yüzey sıcaklığının diğer bölgelere göre 1 ve 11 C° arasında arttığı gözlemlenmiştir. Bunun sebebinin yangın sonrasında yanmış orman alanın albedo değerlerinin düşmesi olduğu (düşük albedo yüzeyde daha fazla güneş enerjisinin absorbe edilmesine yol açar) düşünülmektedir.

dLST ve dNBR parametreleri arasında olası bir ilişkinin olup olmadığını belirlemek için bu değişkenlere korelasyon analizi uygulanmıştır. Bunun sonucunda yüzey sıcaklığı değişimi ile yanma şiddeti arasında yüksek bir korelasyon olduğu (R = 0.8138) görülmüştür. Ayrıca diğer spektral yanma indekslerinden elde edilen dBAI, dMIRBI ve dNBRT'nin dLST verisi ile bir ilişkisinin olup olmadığını görmek için korelasyon analizi gerçekleştirilmiştir. Sonuç olarak dLST ve dMIRBI arasında negatif bir korelasyon (R = -0.7520) olduğu ve dLST ile dNBRT arasında da yüksek bir korelasyonun (R = 0.8567) olduğu gözlemlenmiştir. Ancak dLST ile dBAI arasında herhangi bir korelasyon olmadığı (R = 0) görülmüştür.

Kontrolsüz sınıflandırma işlemi olarak ISODATA algoritması yangın sonrası elde edilen 10 m ve 20 m mekânsal çözünürlüğe sahip Sentinel 2 ve 30 m mekânsal çözünürlüğe sahip Landsat 8 uydu görüntülerine uygulanmıştır. Sınıflandırma

sonucunda yanmış orman alanı Sentinel (10 m) için 972,9 ha, Sentinel (20 m) için 938,61 ha ve Landsat (30 m) için 926,91 ha olarak bulunmuştur (İzmir Orman Genel Müdürlüğü tarafından yapılan arazi çalışmasında yanmış orman alanı 986 ha olarak ölçülmüştür). Kontrollü sınıflandırmada Maksimum Benzerlik ve Destek Vektör Makineleri algoritmaları kullanılmıştır. Maksimum Benzerlik sınıflandırma algoritması sonucunda yanmış orman alanı Sentinel (10 m) için 962,37 ha, Sentinel (20 m) için 963,36 ha ve Landsat (30 m) için 911,34 ha olarak bulunmuştur. Sınıflandırma sonuçlarının doğrulukları ise Sentinel (10 m) için % 96,43, Sentinel (20 m) için % 82,22 ve Landsat (30 m) için % 80,30 şeklindedir. Destek Vektör Makineleri algoritması sonucunda ise yanmış orman alanı Sentinel (10 m) için 991,35 ha, Sentinel (20 m) için 994,65 ha ve Landsat (30 m) için 997,11 ha olarak bulunmuştur. Sınıflandırma doğrulukları Sentinel (10 m) için % 99,56, Sentinel (20 m) için % 97,86 ve Landsat (30 m) için % 97,52 şeklindedir.

Son olarak bir CBS verisi uzaktan algılama verileriyle entegre edilerek eğim ve orman kapalılık haritaları üretilmiş ve bunların orman yangınına ve yanma şiddetine olan etkileri analiz edilmeye çalışılmıştır. Sonuç olarak, % 29 ve % 41 arasındaki eğimin ve % 71 - 100 oranında kapalılığın orman yangınını etkilediği görülmüştür. Ayrıca, sonuçlara göre yine % 29 ve % 41 arasındaki eğimin ve % 71 - 100 oranında kapalılığın çoğunlukla düşük yanma şiddetine neden olduğu belirlenmiştir.

Bu çalışmada, orman yangınlarından etkilenen alanları izlemek için uzaktan algılama ve CBS tekniklerinin başarılı bir şekilde kullanılabileceği gösterilmiştir.

1. INTRODUCTION

In the last century the humankind made great scientific discoveries. It was possible to develop the technology parallel to these fundamental discoveries which eventuate in understanding and analyizing the Earth.

As a result of the industrial revolution, the increasing human population and demand for natural resources lead to a great change on planet Earth physically. Excessive consumption of natural resources and the destruction of nature by man causes disastrous consequences such as global warming. In addition, natural disasters like earthquakes, tsunamis and forest fires necessitate to observe and comprehend the environment by using the information and technology. Remote sensing, the geoinformatics based technology, will help to monitor these environmental problems with its data store created from past to present, and also it can assist to predict and analyze all the disasters may occur on the planet.

Remote Sensing has become one of the most important scientific and technical area with the aerospace technologies that was developed especially after the Wolrd War II. The main purpose of remote sensing techniques is the surveillance of Earth's terresterial landscapes, oceans, and ice sheets by the use of unmanned aerial vehicles (UAVs), airplanes, and satellites [1]. Remotely sensed images are widely used in a range of terresterial, oceanographic, and atmospheric applications, for example forestry, agriculture, mineral exploration, meteorology, and land use/land cover change etc. Satellite images have particular charesteristics which initiate fundamental advantages for studying the surface of Earth. As these images allow to monitor changes in time, and to measure areas, sizes, heights, and depths, they are invaluable [2].

After the development of Geographical Information System (GIS) in the mid 1960s, the integration of remotely sensed data and GIS was used for modeling, analyzing, and mapping the environment. Hence, the use of GIS in remotely sensed data has enhanced the cartographic representation and thematic information. Improving the remote sensing image processing techniques by the integration of GIS can be determined at

numerous stages, such as selecting the region of interest for preprocessing, processing, and image classification [3].

Forest fire analyse is one of the significant applications of remote sensing and GIS integration. An integrated analysis approach of a forest fire is obligatory since the variety of parameters which affect the beginning and spreading of the fire [4]. It can be said that the integration of remote sensing and GIS is the most useful and efficient way to monitor and map forest fires at local, regional, and global scales [5].

In this study, remote sensing and GIS were applied to a forest fire occurred on 1 July, 2017 in Menderes, Izmir for monitoring, analysing, and mapping the results comprehensively by using SENTINEL 2 and LANDSAT 8 satellite images obtained before and after the fire, and a GIS data acquired from a field work.

2. REMOTE SENSING

Remote sensing is the collection and recording of physical data of an object without being in direct touch or contact with that object [2]. In more detail, remote sensing is the science and technology that utilizes the electromagnetic radiation quantitatively and qualitatively which is emitted or reflected by an object without a phyiscal interaction to evaluate and measure the charesteristics of the object remotely.

After the invention of photography at beginning of the nineteenth century the opportunity to record the image of the Earth was possible. Afterwards, physical conceptions of modern remote sensing was revealed associated with discovery of visible part of elecotrmagnetic spectrum in 1800s, infrared radiation discovered by Herschel, ultraviolet by Ritter, microwaves by Hertz; moreover, the electromagnetic theory was developed by James C. Maxwell in 1863 [6].

The fundamental impovements in remote sensing as a scientific area came out after the World War II. Initial remote sensing activities started with automatic photo-camera systems placed in German V2 rockets which was invented by Werner von Braun [7]. The USSR-built SPUTNIK satellite became the very first man made satellite which was launched to space during the Cold War in 1957; furthermore, a new era started for remote sensing which made it possible to attach a film camera to a space vehicle in a desired orbit. This provided an opportunity to explore the Earth, and also the moon and other planets by a series of missions. After the launch of TIROS-1 meteorological satellite in 1960, the first image was taken electronically from a satellite [6]. Remote sensing became an significant tool for civilian usage following the launch of LANDSAT 1 (former ERTS) on 23 July, 1972. Global remote sensing satellite systems that cover the entire Earth and offers a broad-scale data were arised in the 1990s with the Terra-1 satellite [2]. The milestones in the history of remote sensing are shown in Figure 2.1.
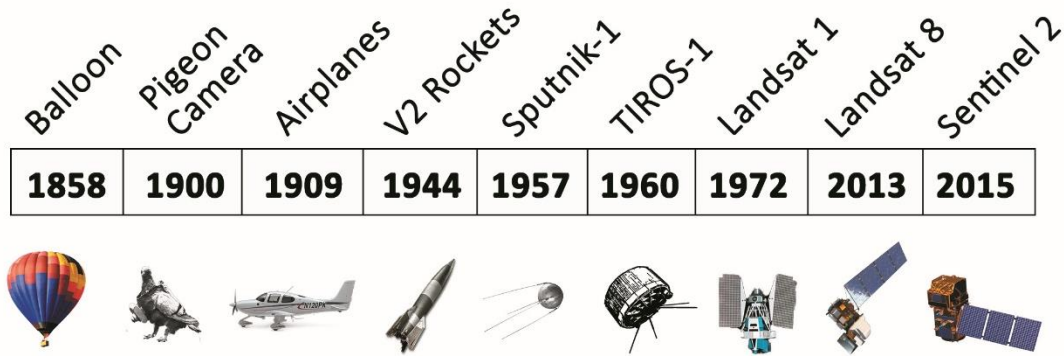
Figure 2.1 : Evolution of remote sensing systems.

2.1 Principles of Remote Sensing

Although the definition of remote sensing contains numerous technologies in a broad sense, all remote sensing technologies are based on certain basic concepts and contain the same fundamental components. The main constituents in the system are target, energy source, transmission path and a sensor (Figure 2.2).
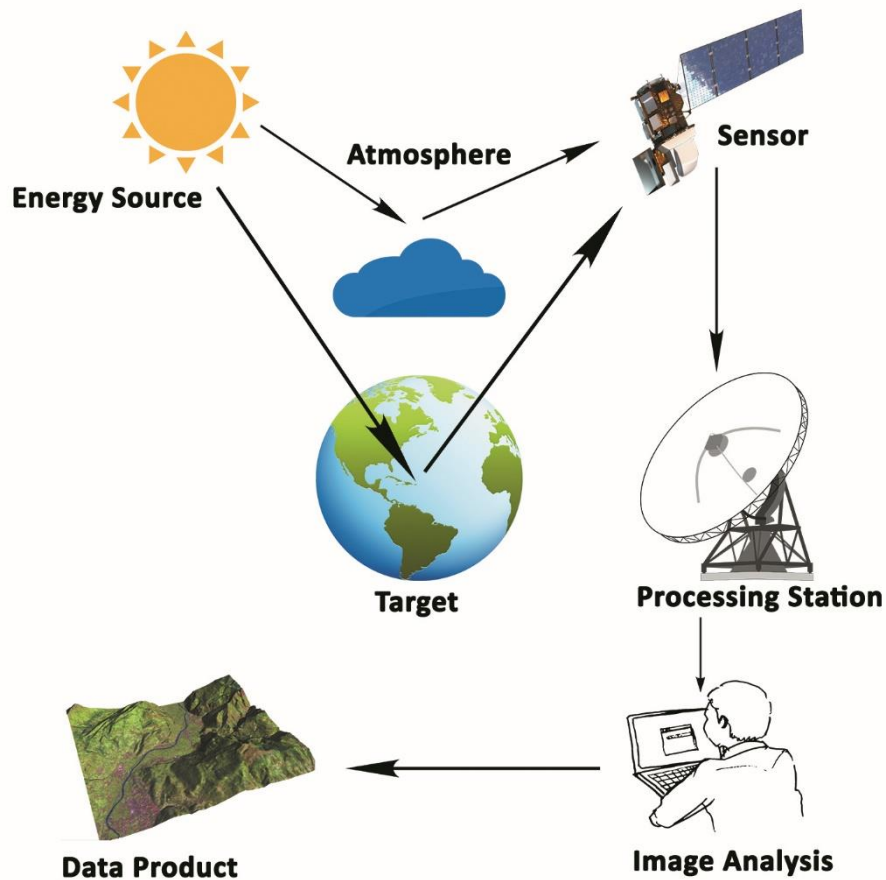
Figure 2.2 : Remote sensing process and its components.

Detection and discrimination of objects or surface features mean detecting and recording of radiant energy reflected or emitted by objects or surface material. Various objects reflect diversified amount of energy in different bands of the electromagnetic spectrum according to the characteristic of material (structural, chemical, physical), surface roughness, intensity, incidence angle and wavelength of radiant energy. In brief, remote sensing consists of the following six steps [1].

1) The energy source that generates the electromagnetic radiation which interacts between the remote sensing platform and the surface of Earth. The principal energy source for remote sensing is the Sun.

2) Surface of the Earth which includes vegetation, water, soil, ice, and settlement areas etc. Emitted or reflected energy of these surfaces are sensed by the sensor.

3) Platform and Sensor. Basically, the platform is the vehicle carrying the remote sensing devices such as power supply, attitude determination and control, and communications. The sensor is the instrument that detects the electromagnetic radiation reflected or emitted from an object.

4) Ground receiving station that accumulates all the data electronically and stores the data.

5) The analyst who analyses the data and transforms the image into cartographic infromation.

6) The last step is the consumers which make use of the processed data for various applications.

2.2 Electromagnetic Radiation and Spectrum

Electromagnetic radiation (EM) is the flow of energy at the speed of light through a vacuum or a material medium in the form of the electric and magnetic fields (Figure 2.3). The laws of electricity and magnetism was explained by James Clerk Maxwell in the 1860s. He revealed also that light was a form of electromagnetic radiation [6]. The quantum theory of EM radiation was revealed by Max Planck and Albert Einstein.

Energy in the sense of particles is always thought as quantum which propagate in the same direction and velocity as the waves. This condition is a notion in quantum pyhsics that the electromagnetic radiation moves like a particle rather like a wave [6]. The energy of each particle is called a photon. The energy carried by a waveform for a single photon is expressed in equation (2.2).

$$E = hf = h\frac{c}{\lambda} \tag{2.2}$$

Where h is the Planck constant, f is the frequency, c = 299792 km/s is the speed of light, and λ is the wavelength. As energy is proprtional to frequency and inversly proportional to wavelength, an increase in wavelength leads to a decrease in energy.
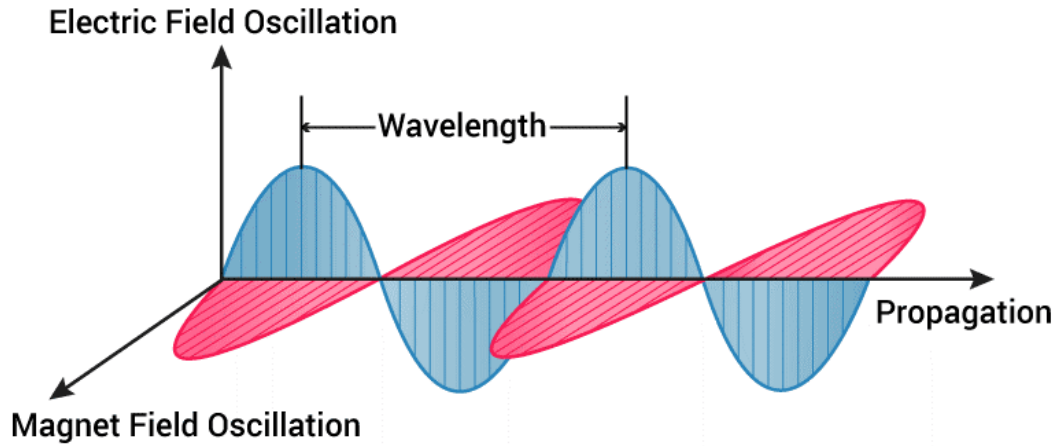
Figure 2.3 : Electromagnetic radiation [8].

All objects emit electromagnetic energy, because of the kinetic energy of molecules inside them as having a temperature above absolute zero. The distribution of this energy does not change regularly with the change of wavelength. A blackbody is a theoretical ideal radiator which absorbs and re-emits all energy incident upon it. The quantity of radiation emitted by the blackbody is based on its absolute temperature [6]. Max Planck calculated the spectral radiance of this blackbody radiation which known as the Planck formula (equation (2.3)).

$$L_\lambda = \frac{2hc^2}{\lambda^2 \, (exp(hc/\lambda kT)-1)} \tag{2.3}$$

Where k is the Boltzman constant.

The equation (2.3) can be approximated at sufficient long wavelengths as equation (2.4).

$$L_\lambda \approx \frac{2kTc}{\lambda^4} \tag{2.4}$$

If the object is an ideal blackbody, the energy radiation is convenience to the Planck equation. Moreover, the total radiation emitted by a blackbody is explained by the

Stefan-Boltzmann law [7]. Basically, the integration of the Planck equation calculates the total radaince of a blackbody radiation of whole wavelengths (equation (2.5)).

$$L = \int_0^\infty L_\lambda d\lambda = \frac{2\pi^4 k^4}{15c^2 h^3} T^4 \tag{2.5}$$

To calculate the spectral exitance M, equation (2.5) is multiplied with π. The compact form of Stefan-Boltzmann law is given in equation (2.4).

$$M = \sigma T^4 \tag{2.4}$$

Where $\sigma = 5.67 \times 10^{-8}$ Wm^{-2}K^{-4} is demonstrated as the Stefan-Boltzman constant. Figure 2.4 shows the spectral radiance of a blackbody radiation.
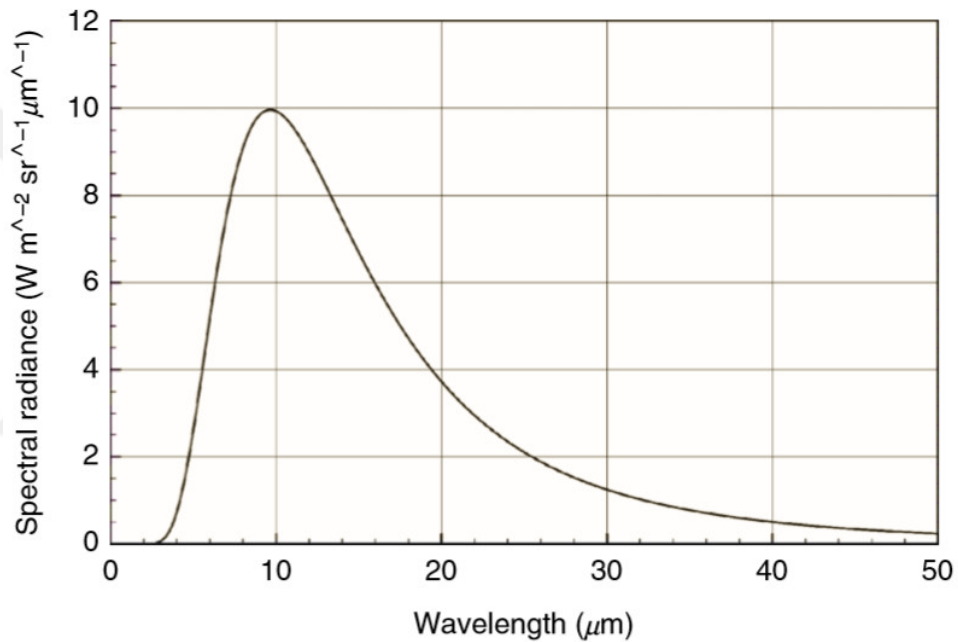
Figure 2.4 : The spectral radiance of blackbody radiation [6].

The wavelength where the blackbody radiation is maximum is explained by the Wien's displacement law and it is shown in the equation (2.5).

$$\lambda_{max} = \frac{A}{T} \tag{2.5}$$

Where $A = 2.898 \times 10^{-3}$ mK is the Wien's displacement constant and T is the temperature.

Electromagnetic spectrum is the classification of entire form of electromagnetic radiation (Figure 2.5). It is a continuous energy medium which has a wavelength from 10^{-10} µm (cosmic rays) to 10^{10} µm (radio waves). Remote sensing deals specifically

with 0.3 – 15 μm optical wavelengths and 1 – 1000 mm microwave wavelengths. In detail, these particular spectral regions are as the following.

1) The ultraviolet region (0.03 – 0.4 μm) : Because of the absorption by the Earth's atmosphere, the ultraviolet spectrum is not generally used for remote sensing applications. Only the wavelength between 0.3 – 0.4 μm (also known as photographic ultraviolet) are utilized for practical purposes.

2) The visible region (0.4 – 0.7 μm) : The visible part of the spectrum consist of three segments which was revealed by Isaac Newton in 1660s. These primary colors are defined as nearly 0.4 – 0.5 μm (blue), 0.5 – 0.6 μm (green), and 0.6 – 0.7 μm (red). It has a fundamental importance for remote sensing applications.

3) The infrared region (0.7 – 1000 μm) : This region is composed of near infrared (NIR) (0.7 – 3 μm), thermal infrared (TIR) (3 – 14 μm), and far infrared (15 – 1000 μm) regions. The significance of NIR is due to the identification of vegetation health status. Furthermore, TIR region is crucial for determining of land surface temperature and also soil moisture.

4) The microwave region (0.1 – 100 cm) : These wavelengths can be demonstrated with active sensor systems which are independent of atmoshperical effects such as cloud, fog, and rain [7].
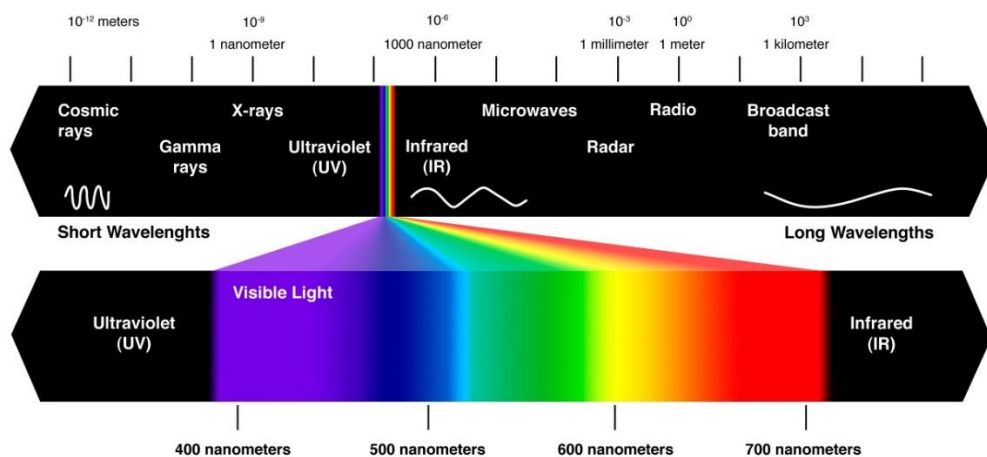
Figure 2.5 : Electromagnetic spectrum [9].

2.3 Interaction with Earth Surface Materials

When the electromagnetic radiation reaches to the Earth surface without being absorbed or scattered in the atmosphere, it interacts with the objects in three different ways; i.e. reflection, transmission, and absorption (Figure 2.6). The proportion of the electromagnetic radiation that each type of interaction receives depends mainly on three factors which are, the compositional, biophysical, and chemical properties of the surface material; the wavelength, frequency of the incident radiation; moreover, the angle at which the incident radiation strikes the surface [10].

Transmission   **Reflection**   **Absorption**
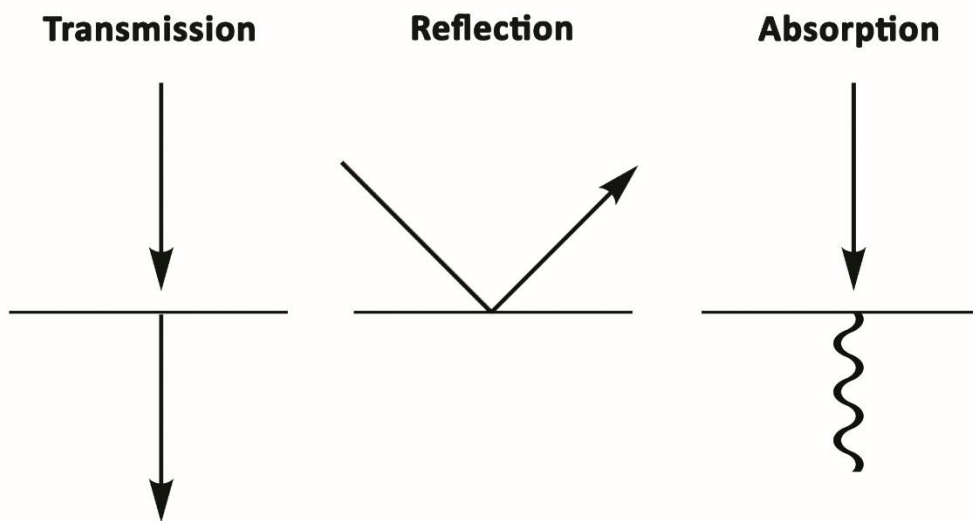
Figure 2.6 : Earth surface interaction of electromagnetic radiation.

The amount of reflected energy of surface materials is significant for remote sensing. The ratio of the amount of reflected radiation to the total radiation is defined as albedo [7]. Therefore, if an object reflects a large part of the incoming radiation, it will have a high value of albedo (Figure 2.7). In equation (2.6) the mathematical formula of albedo is demonstrated.

$$Albedo = \left({Reflected\ radiation}/{Total\ Radiation} \right) \times 100 \qquad (2.6)$$

The objects with the highest albedo ratio among the Earth's surface materials are snow, glacier, and sand; on the other hand, the lowest albedo values are soil and forest areas.
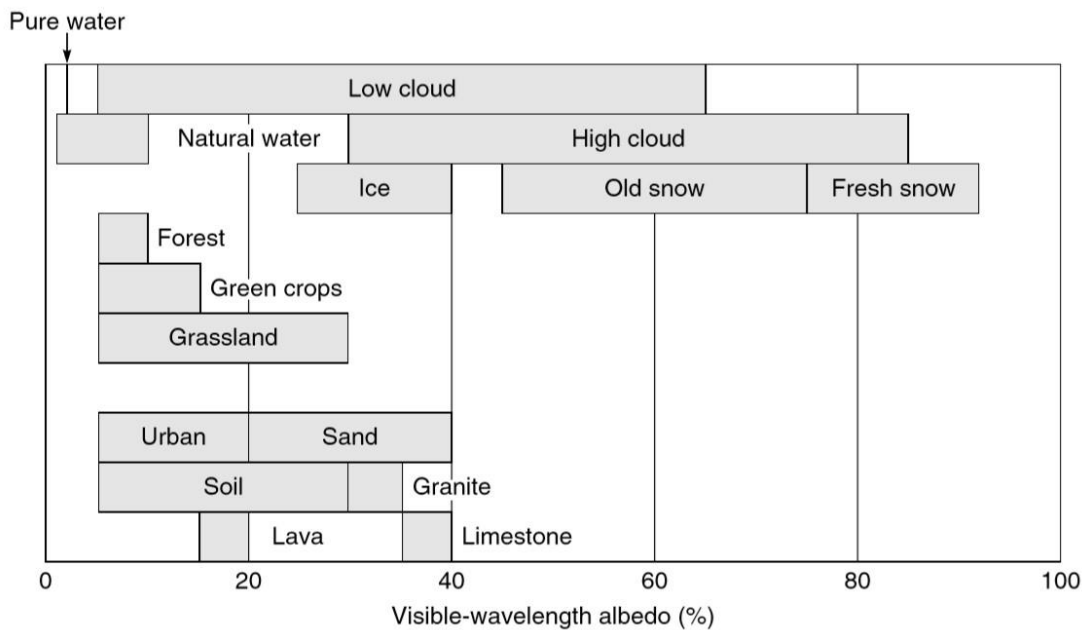
Figure 2.7 : Albedo values of different surface materials in visible wavelength [6].

2.3.1 Spectral reflectance properties

As it is known the main source of electromagnetic energy is the Sun. The internal temperature of the Sun is approximately 20 million K; however, only the photosphere which is the surface of the Sun is observable. Furthermore, its temperature is nearly 6000 K. The most of the solar radiation exitance that spreads on a wavelength range from 0.3 to 3 μm (the exitance peaks at 0.5 μm) can be computed by the use of radiation laws [1].

All the materials on the surface of Earth are transmit, reflect or absorb the EM radiation in various ways as mentioned previously. The wavelength of EM radiation is also effecting the reflectance properties. As a result, the differences in reflectance properties enable to characterise the different surface materials by analysing their spectral reflectance curves. The spectral reflectance curves are the graphs of different surface materials depend on a function of wavelenghts [45].

2.3.1.1 Spectral reflectance properties of vegetation

One of the principal and fundamental problem in remote sensing is the specification and spectral properties of vegetation canopies. The signal which is detected by the sensor is effected by external factors, and bio-chemical and bio-physical canopy features. The spectral refelctions of vegetation canopy changes depending on the wavelength. Pigmentation, physiological structure and water content have a significant

10

effect on vegetation canopy while reflection, transmission, and absorption (Figure 2.8). Leaf's spectral reflectance can be affected by the health, age of the leaf, and nutrient stress [1].

In the visible region, the pigments contained in the plants absorb the energy for photosynthesis. Especially in the blue and red regions on wavelengths nearly 0.45 μm and 0.65 μm respectively the energy is absorbed because of the chlorophyll; on the other hand, it is reflected by green region at approximately 0.55 μm wavelength. Hence, healthy leaves appear as green (Figure 2.9). The reason for different leaf colors in the autumn is the red and blue pigment xanthophyll which gets dominant with leaf aging [1].
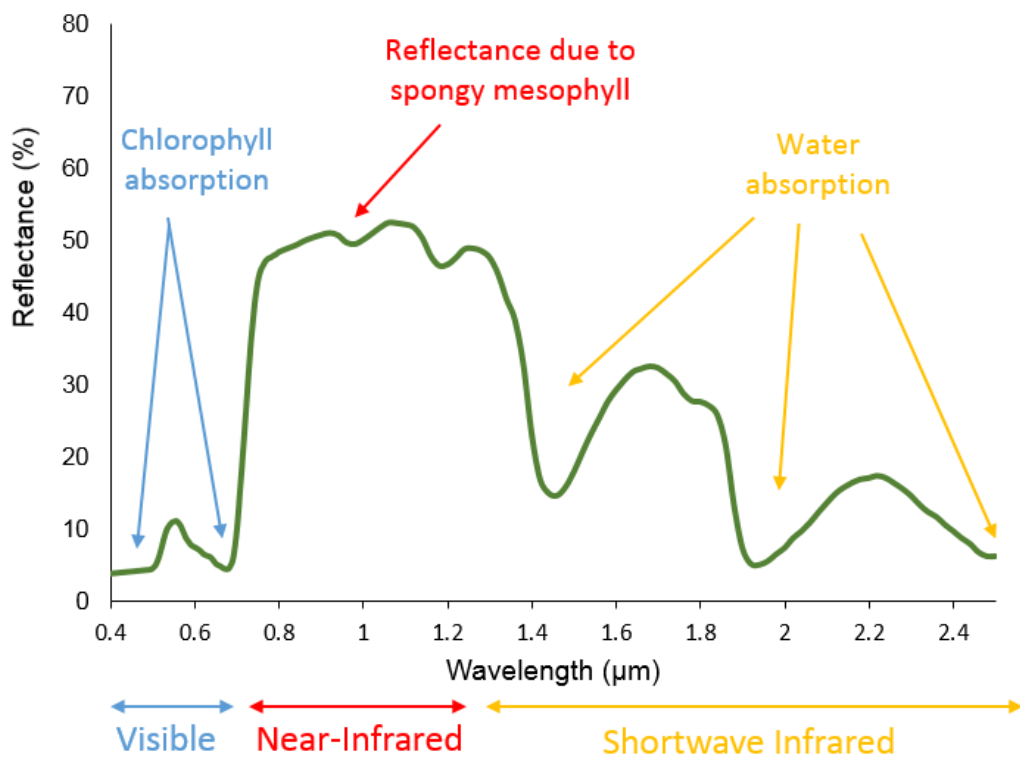
Figure 2.8 : Spectral reflectance of vegetation [11].

In the near infrared region, because of the cellular structure of the vegetation, especially the spongy mesophyll, the reflectance peaks for a healthy vegetation and can be easily identified by difference of NIR and visible regions [11]. Therefore, near infrared spectrum is fundamental for vegetation biodiversity studies. The common effects of the leaf pigments and the physiological structure give the all healthy green leaves the characteristic of reflective properties.

The reflection in the shortwave infrared region depends on the amount of water, and also the thickness of the sheets. Reflection decreases since the amount of water increases, so absorpiton remains [7]. Solar radiation at 1.45 μm and 1.95 μm are strongly absorbed by water and also the radiation at these wavelengths is also absorbed in the atmoshpere before reaching the surface [1].
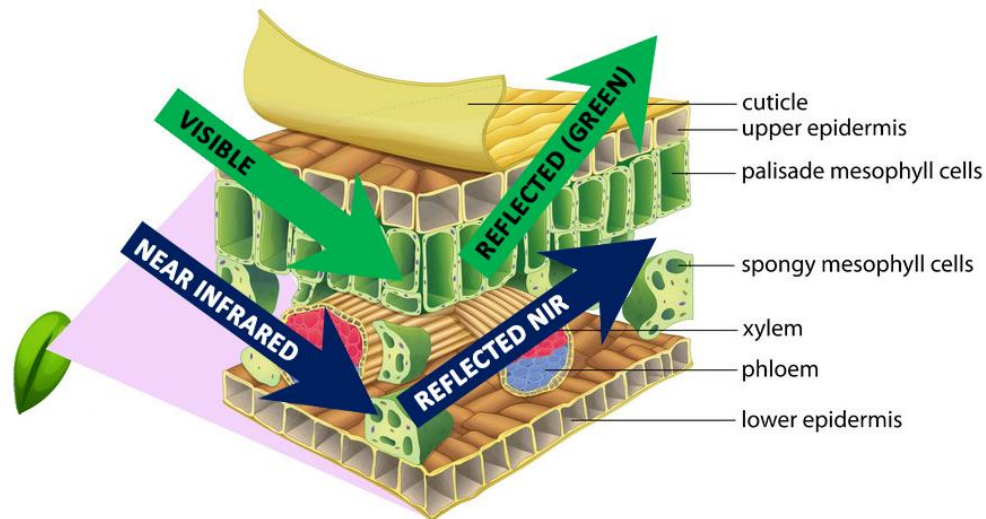
Figure 2.9 : Interaction of the electromagnetic radiation with a healthy leaf.

2.3.1.2 Spectral reflectance properties of soil

The general charesteristics of the spectral reflection curves of the soils are raised due to the increased wavelength of the reflection (Figure 2.10).

The electromagnetic energy is transmitted slightly trough the soil differently than vegetation. The biogeochemical substances are the reason for the reflected and emitted energy by the soil [1]. In general, spectral properties of soil is depending on the water content of the soil, the type and amount of minerals forming the soil, surface roughness and the organic matter content [7].

Generally, soils which contain quartz highly reflect the incoming radiation almost in all regions of electromagnetic spectrum, and soils with water content absorps the near infrared and short-wave infrared radiation; on the other hand, soils that include high organic matter absorbs the visible spectrum of electromagnetic spectrum. The reason for the water absorption bands at 1.4 μm and 1.9 μm is because of the atomic vibrational processes [1].
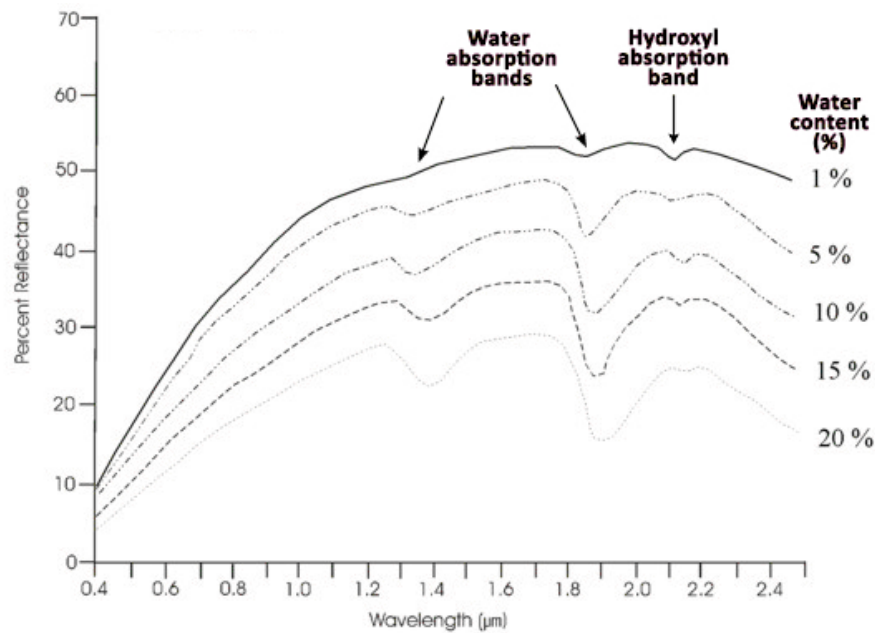
Figure 2.10 : Spectral reflectance of soil.

2.3.1.3 Spectral reflectance properties of water

Different from the other surface materials, water absorps or transmits most of the received solar radiation. In the visible spectrum clear water has the highest reflectance at the blue wavelenghts; however, it is absorped strongly in the near and shortwave infrared regions (Figure 2.11). Because of the difference from vegetation and soil in the spectral reflectance, it is easier to identify water bodies on remotely sensed images.
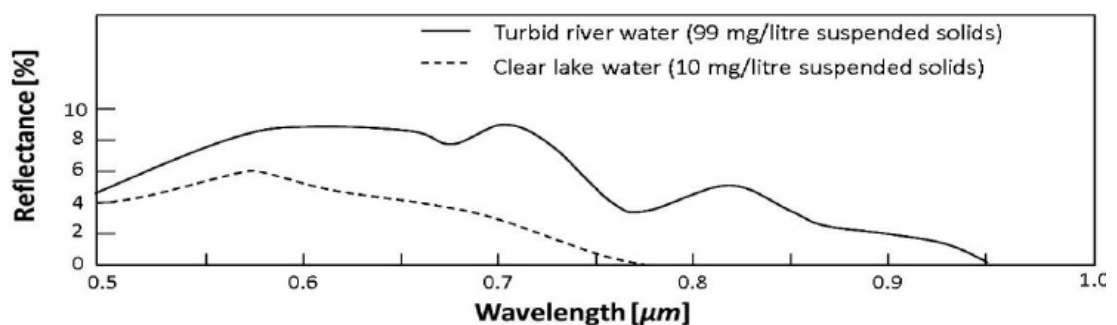
Figure 2.11 : Spectral reflectance of water [12].

The factors that are affecting the reflectance properties of a water body are water depth, the content of the water, and surface roughness of water [7].

As the water depth increases, the absoprtion of incoming energy will also increase. Mapping the coastal areas is also based on this phenomenon.

13

If the amount of water contents especially the chlorophyll will rise, it will decrease the reflectance of the blue band. Accordingly, the amount of chlorophyll can be evaluated by spaceborne systems.

Lastly, the diffuse scattering and reflection which can be harm to the internal detectors of the sensors, since the Sun glints or strong signals are due to the water surface roughness.

2.3.2 Emission properties of earth surface materials

As mentioned previously all objects with a temperature above absolute zero emit energy and the radiation is mostly detected by the passive remote sensing systems. The spectral radiant exitance (M) is most distinct at 8 – 14 μm spectral region on the EM spectrum according to Planck's and Wien displacement laws, taking into consideration that Earth's temperature is nearly 300 K.

Emissivity (ε) is the ratio of spectral radiance of a material to a perfect emitter (blackbody) at the same temperature. It is relative to the spectral radiant exitance (M) of an object and acquires values between 0 and 1. If a material absorps and emits a major proportion of the incoming radiation, it specifies a high emissivity (near to 1). Table 2.1 shows the emissivity values of some surface materials. Estimation of land cover radiant exitance (M) can be determined with measuring the emissivity by knowing the kinetic temperature of materials [1].

Table 2.1 : Emissivity (ε) values of different surface materials.

Surface Materials	Emissivity (ε)
Vegetation	0.98
Soil	0.90
Water	0.99
Metal	0.16

There are some different parameters related to emission properties of objects such as thermal capacity, thermal conductivity, thermal diffusivity, and thermal inertia.

- Thermal capacity (C) is the capacity for the heat storage.

- Thermal conductivity (k) is ratio of transmitted heat on the land surface.

- Thermal diffusivity (K) is the measurement of how surface temperature alters straightly through heat conduction.

- Thermal inertia (*P*) is the resistance of an object to the fluctuation on the temperature. It is relevant with the others. Figure 2.12 demonstrates the thermal inertia of different Earth surface materials [1].
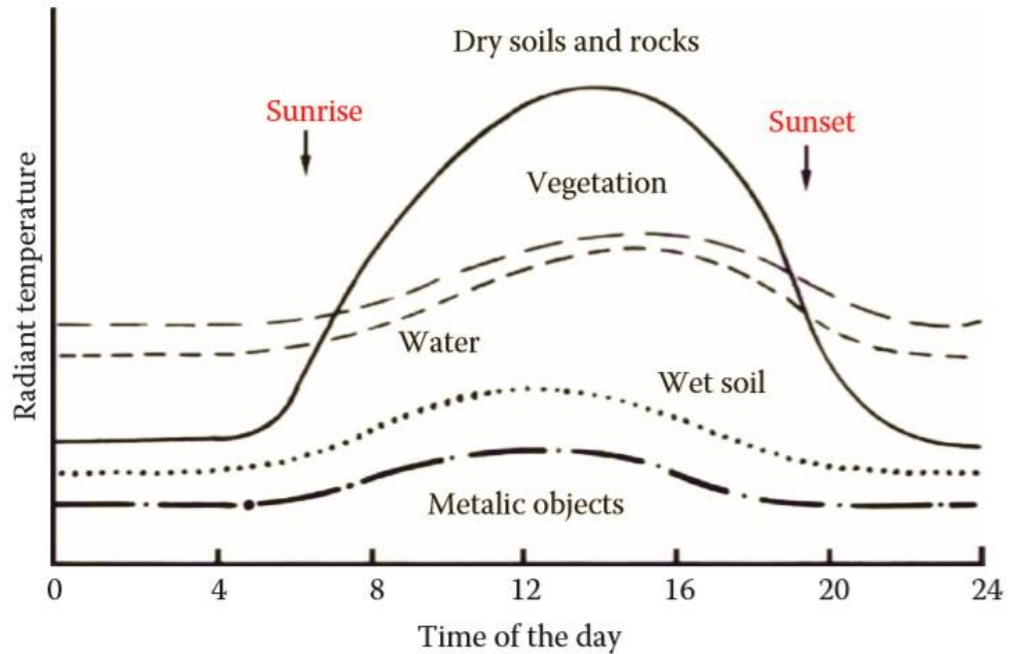
Figure 2.12 : Thermal inertia of different Earth surface materials [1].

During the photosynthesis process plants absorp a large quantity of incoming radiation; therefore, it is complex to specify the emission properties of vegetation. To protect the energy balance plants re-emit this energy during the night. Furthermore, vegetations have a high thermal inertia due to the water content. Evapotranspiration is also a fundamental parameter for vegetation emission. During the evapotranspiration process the sensible heat of vegeatation decreases; hence, plants are cooler during the day than the surrounding surface materials. However, they are hotter than the surrounding objects at the night time due to the re-emition of the energy. Health problems on vegetation decrease the difference of day and night time temperature. Density and canopy are the significant factors that effects the emissivity of vegetation.

The emission properties of soil are mostly controlled by the soil moisture. The water content (0-2 cm) in soils is inversely relative to daily minimum and maximum surface soil temperatures. An increase in the moisture content of a soil will increase the thermal inertia. Accordingly, soils with high water content will appear cooler than dry

soils at day time and warmer at night time. The differences in temperature during day and night is also highly dependent on organic matter content.

Water has a higher thermal inertia than the other mentioned surface materials because of the convection movements which lead to absorption and transmission of the incoming solar radiation. Therefore, the water temperature is relatively stable. The importance of the observation of water emission is beneficial for the climatology and meteorology.

3. REMOTE SENSING & GIS INTEGRATION

After the developments in computer technology and impression of the quantitative revolution in geography, Geographic Information System (GIS) appeared in the mid-1960s. Computers was adapted to cartography, geodesy and surveying for the potentiality reducing the time for mapping and cost of effectiveness. Altough parallel progresses of GIS took place in Europe, North America, and Australia, the first real GIS was the Canada Geographic Information System (CGIS) designed for computer based map surveying in the early 1960s. Afterwards, the DIME (Dual Independent Map Encoding) program was generated by the US Bureau of the Census for planning all the streets in US to support the census records. Harvard University's Laboratory of Computer Graphics also made a fundamental program for spatial analysis named ODYSSEY GIS in the late 1970s. Moreover, the first map which was made on computer was published by the British Geological Survey in 1973 [3, 23].

Remote sensing was also significant for the improvement of GIS as a technology and also a data source. After the World War II, the military aerospace technology was developed with spy satellites which prompt governments to improve the GIS technology. For this purpose, image classification and pattern recognition technologies arised for military applications. However, the development of GIS in the modern sense originated during the Cold War in 1980s [23].

Geographic Information System is defined as a geoinformatics based software package which is specifically designed for applying broad-scaled tasks for geographical purposes. Data input, storage, processing, analyze, managing, and display are the basic tasks of a GIS system [3]. There are several application areas for GIS such as transportation, public safety, real estate, surveying, and natural resources etc. Furthermore, mathematics, remote sensing, photogrammetry, geography, and computer technology are the scientific and technological areas that evolved the GIS [24].

Remote sensing and GIS are integrated in three different ways as follows [3]:

- Remote sensing is utilised to obtain data for the use of GIS.

- To improve the remote sensing data, data acquired from GIS is used as ancillary information.

- For modeling and analysis remote sensing and GIS are utilised together.

Firstly, to generate GIS layers, remotely sensed images can be used to extract the thematic information. Maps can be created by digitizing the remotely sensed data which provides a number of thematic categories such as settlement areas, forest areas, soil, and water bodies. In addition, satellite images can be classified and entered into the GIS layers. Remote sensing can also be used to extract the cartographic information to integrate with GIS. For example, lines, polygons, and other geometric properties can be acquired from remotely sensed data. Furthermore, one of the most important problem in GIS databases is updating the data. For this purpose, remote sensing is utilised to update the GIS in a cost-effective way. By using remote sensing data in GIS, change detection can be determined too. Figure 3.1 demosntrates the integration of GIS layers with a remotely sensed data.
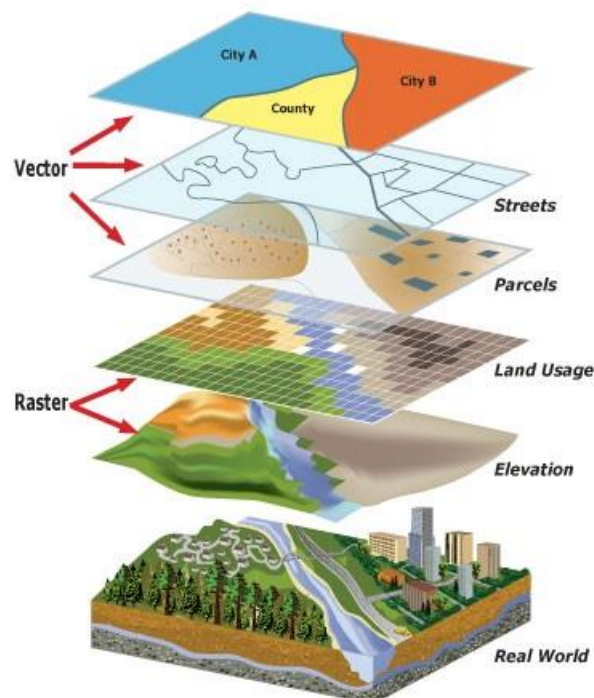
Figure 3.1 : Integration of GIS and remotely sensed data [25].

18

GIS can be used as ancillary data during the geometric and radiometric correction of remotely sensed satellite image. For the geometric correction, vector points, DEMs (Digital Elevation Models), and area data can be acquired from GIS. In addition, DEMs can also be utilised as eliminating the radioametric effects from the satellite image. An another use of GIS in remote sensing is for the selection of the area of interest which is significant for image processing especially for image classification.

Thirdly, remote sensing and GIS are utilised together that involves simple spatial queries, the cover of thematic and statistical attributes from remote sensing and GIS, and the production of multiple-view expert systems. Third level integration of remote sensing and GIS is one identical system in which both raster and vector layers are processed interchangeably [46].

Consequently, GIS supplies a comfortable environment for remote sensing for managing, analyzing, and displaying the data [25].

4. REMOTE SENSING OF FOREST FIRE STUDIES

According to Valero et al. (2018), the rate of fire spread which is relevant to topography, weather, and vegetation can be determined by the integration of remote sensing and GIS. In this study, rates of spread (ROS) are computed by the use of Digital Elevation Model (DEM), and the fire spread is shown on a map. In addition, the correlation between ROS, intensity, topography, and vegetation type was studied. For this purpose, SRTM 30 m DEM, OpenStreetMap, and fuelbed dataset were used for the forest fire occured in Vall-Lloobrega, Catalonia, Spain in March 2014. Results have shown that ROS is strongly related with some fuel models such as 2 m tall mature shrubs and timber litter. Moreover, the positive correlation between ROS and slope is not linear [26].

As Adab et al. (2013) stated, fire risk can be identified by the use of remote sensing and GIS techniques. Thus, Structural Fire Index (SFI), Fire Risk Index (FRI), and Hybrid Fire Index (HFI) are used to display the fire risk of Golestan, Iran. MODIS, ASTER DEM, and anthropogenic data are integrated to calculate the indexes. For estimating the fire risk in stated area the probability distributions are used. Furthermore, the risk is modeled from these indexes, and it was classified into three levels; low, moderate, and high. As a result, 53% of total area is highly at fire risk for SFI, %42 for HFI, and %36 for FRI. The accuracy of the SFI, HFI, and FRI indexes are identified as 68%, 76%, and 64% respectively [27].

As emphasized by Jaiswal et al. (2002), for identifying and mapping the forest fires, and determining the fire risk zone, remote sensing and GIS are significant. Indian Remote Sensing Satellite (IRS) and GIS data which was derived from field information was utilised to map the fire risk zone of Madyha Pradesh, India. Fire Risk Index was used for this study. Some parameters like vegetation type, slope, proximity to settlements, and distance from roads which are responsible for forest fires was defined for the integration of remote sensing and GIS data. According to the results, the fire sensitivity of vegetation type was very high for dry mix and low for agriculture, the

fire sensitivity of proximity to settlements; was high under 1000 m, and low from 2000 to 3000 m, the fire sensitivity of distance from roads; was very high under 100 m, and low from 300 to 400 m, the fire sensitivity of slope; was low from 0 to 3 %, and very high above 35 %. Accordingly, the fire risk of 20 % of total area was very high; on the other hand, the fire risk of 50 % of total area was low [28].

According to Vlassova et al. (2014), the relevance of land surface temperature (LST) and burn severity can be specified by the use of satellite images. Totally fifteen Landsat 5 TM satellite images are used to observe the 27 post fire months of the forest fire occured in Extremadura, Spain. To determine the burn severity, the differenced normalized burn ratio (dNBR) was utilised, and the mono-window algorithm was ustilised to obtain the LST. Consequently, shortly after the fire burned areas was approximately 7.6 °C warmer than unburned areas, and the statistical results have indicated that LST differences are strongly relative to burn severity in the fire area. In addition, the relationship is still determinable after two years from the fire [29].

As mentioned by Quintano et al. (2015), the relationship between land surface temperature (LST) and burn severity can be determined by remote sensing techniques in Mediterranean forests. For this study, six Landsat 7 ETM+ and ASTER DEM data was utilised to estimate the LST by the use of single channel algorithm. For the burn severity, Composite Burn Index (CBI) was performed. Firstly, the LST and CBI calculation was applied, and then statistical calculations was carried out for the correlation analysis. High correalation was observed between post fire LST and CBI ($R_{adj} > 0.85$). In addition, post fire LST was also affected by ecological variables such as climate (relative humidity, wind speed), topography, and forest species [30].

As Guangmeng and Mei (2004) indicated, land surface temperature (LST) determined by remote sensing techniques can be used to identify forest fire risk. MODIS data was utilised for this study to estimate the fire risk with a developed neural network method on two forest fires occured in Northeast China. For the determination of LST two different methods was performed which are split-window, and day/night algorithm developed by the authors. LST was calculated five days before the fire with twelve satellites images of these two forest fires. As a result, pre-fire LST values are increasing day by day up to the fire day. The rising trend begins especially three days before the fire. Furthermore, the fire potential index (FPI) was also used for acquiring the fire risk, and the observations demonstrated that FPI is also increasing day by day

till to the fire day. The result of FPI have shown that LST is also suitable for estimating the fire risk zone [31].

As research by Anitha et al. (2013) shows, land surface tempeature (LST) can be ustilised to identify forest fires from satellite imagery. For this purpose, k-mean clustering and haar wavelet methods are performed on 312 NASA satellite images to specifiy the mean wavelengths of abnormal temperature distribution. Generated algorithm works basically as follows; calculating the LST, denoising, k-means clustering, haar wavelet transform, computing the mean wavelength; if the mean wavelength is above or equal to 10.14 then there is a forest fire, if not there is no forest fire. As a result, with a 89.5 % accuracy the algorithm was performed succesfully [32].

According to Norton (2008), burn severity determination can be performed by burn indexes in forested ecosystems and steppes. Landsat ETM+ and SPOT 5 multispectral satellite images are used to calculate the indexes like SAVI, MSAVI, NDSWIR, pNDSWIR, dNDSWIR, NBR, dNBR, RdNBR, rModNDVI, and modified NDVI in the ecosystem of Clark County, USA. Three different categories for burn severiy (unnburned, moderate, high) are stated. Consequently, the overall accuracy of Landsat ETM+ dNBR, RdNBR, NDSWIR, MSAVI, and SAVI indexes are 66%, 73%, 58%, 66%, and 67% respectively, and the overall accuracy of SPOT 5 dNDSWIR, rModNDVI, pNDSWIR, MSAVI, and SAVI indexes are 65%, 67%, 69%, 67%, and 71% respectively [33].

As Sunar and Özkan (2001) stated, forest fire analysis can be determined by remotely sensed data and also GIS techniques. A forest fire occured in Muğla, Turkey was observed by digital image processing methods like classification, spectral profile analysis, and vegetation indices. A GIS data was also utilised from forestry and topographical maps, and meteorological data. Two different classification methods which are conventional and neural classification, and NDVI index are performed on the satellite images (Landsat ETM+ acquired before the fire, and IRS-1c and SPOT HRV acquired after the fire). As a result, the spectral profile of Landsat ETM+ satellite image is normal; on the other hand, the spectral curve has a different property in the IRS-1C satellite image because of the forest fire. These two graphs made it easy to identify burned and unburned areas. Burned area was calculated as 6290 ha from the conventional classification method, and 6294 ha from the neural classification method. However the burned area was measured as 7094 ha by the regional Forestry Chief

Directorate. There are three major reasons for obtaining different results than the regional Forestry Chief Directorate. First of all, the boundaries of the burned area was calculated using planimetric methods from helicopter or by field work. Secondly, on the study area some parts are not forest class but they were marked as burned forest area on the thematic map generated by the Forestry Chief Directorate. Lastly, remote sensing detects and observes the vegetation area in more detail than field works because of the synoptic view advantage[34].

5. EARTH OBSERVATION SATELLITES USED IN THIS STUDY

Satellite is a natural object (moon etc.) that moves around a planet in space; moreover, it is also be identified as a piece of equipment that is sent into space around the Earth to receive and send signals or to collect information.

Platforms for remote sensors can be set on the ground (ladder, tall building, crane etc.), on a balloon or an aircraft, and also on a spacecraft or satellite outside of the Earth's atmosphere [13]. Remote sensing is generally focalized on spaceborne systems such as satellites. Figure 5.1 specifies the different remote sensing platforms and their altitudes.
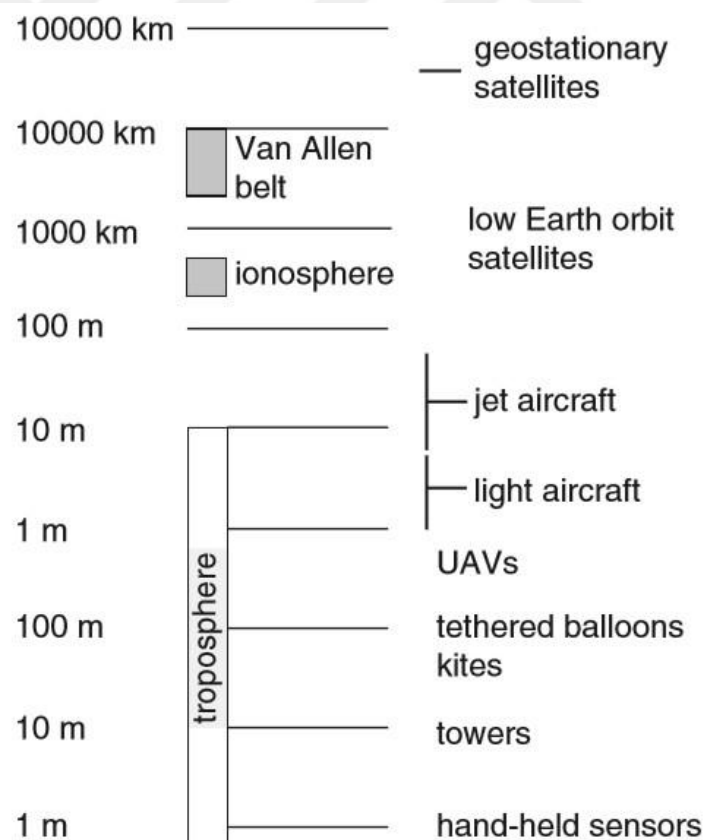

Figure 5.1 : Remote sensing platforms and their altitudes on Earth's surface and atmosphere [6].

Altough the design of spaceborne remote sensing systems are more expensive than airborne or ground systems, there are some advantages such as observing broad areas, synoptic view, speed, reduce of field work etc.

The journey into space began with the Sputnik 1 which is the world's first orbital spacecraft, orbited the earth for three months, launched by the Soviet Union at October 4, 1957. [14] The Television and Infrared Observation Satellite (TIROS), the first earth observation satellite for meteorological purposes operated by NASA, was launched on April 1, 1960 [2]. Furthermore, the first remote sensing satellite launched was Earth Resources Technology Satellite ERTS - A (Landsat 1) on July 23, 1972 by NASA.

5.1 The Landsat Program

NASA started methodical researches to place remote sensing instruments on aircrafts during the Apollo missions in 1960s. Afterwards, Earth observation satellite program was commenced in 1965. These investigations became reality with launch of Landsat 1 in 1972 [15].

The Landsat ("Land Satellite") program has provided uninterrupted information about the surface of Earth since 1972 and created a large satellite imagery archive which performs a service for Earth observation applications [2, 14]. In the view of such information, Landsat program promotes to research on land cover/use change, geology, forestry and agriculture etc. Table 5.1 demonstrates the characteristics of the Landsat program.

Table 5.1 : Characteristics of Landsat missions [15].

Satellite	Launch Date	Sensors	Orbit Height (km)
Landsat-1	23.07.1972	RBV, MSS	900
Landsat-2	22.01.1975	RBV, MSS	900
Landsat-3	05.03.1975	RBV, MSS	900
Landsat-4	16.07.1982	MSS, TM	705
Landsat-5	01.03.1984	MSS, TM	705
Landsat-6	05.10.1993	ETM	705
Landsat-7	05.04.1999	ETM+	705
Landsat-8	11.02.2013	OLI, TIRS	705

5.1.1 Landsat 8

Landsat 8 was launched on February 11, 2013 by the collaboration between NASA and the U.S. Geological Survey (USGS) to obtain measurements of the Earth's radiation in the visible, near infrared, short wave infrared, and thermal infrared regions [16]. Landsat 8 is assembling substantial data and digital images for utilizing in science, agriculture, geology, oceanography, education, etc. It supplies iterative achievement of high resolution multispectral data of the Earth's surface globally.

Landsat 8 has two sensors which are Landsat 8 Operational Land Imager (OLI) and Thermal Infrared Sensor (TIRS).

The OLI sensor was built by the Ball Aerospace & Technologies Corporation, and the TIRS sensor was built by NASA Goddard Space Flight Center (Figure 5.2). The OLI and TIRS sensor sense the images simultaneously [17].
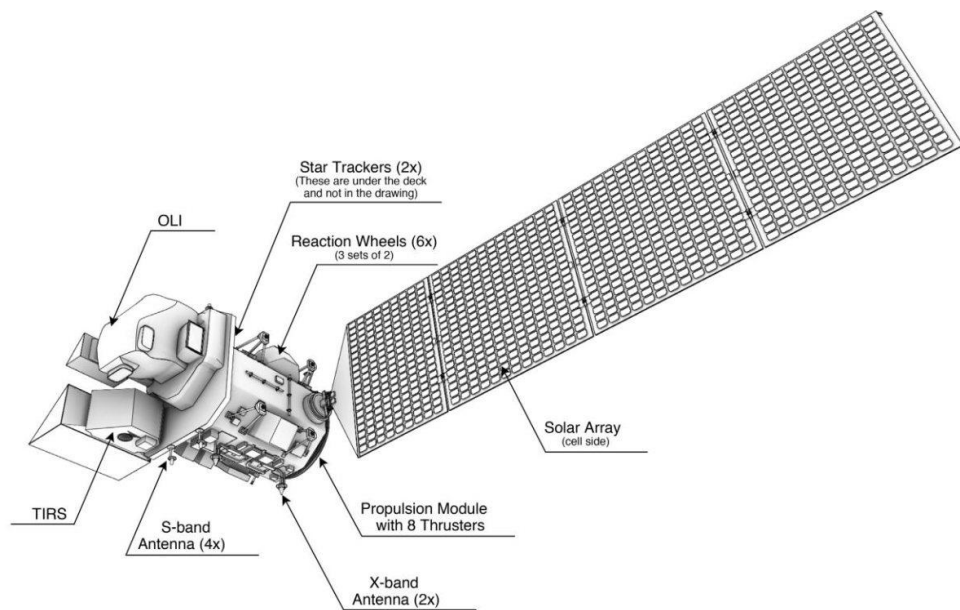
Figure 5.2 : Landsat 8 OLI & TIRS [17].

The Landsat 8 satellite has an orbit which is near-circular, near-polar, and sun-synchronous and its altitude is 705 km. Its ground track repeat cycle is 16 days.

The Operational Land Imager (OLI) is working in the visible, near infrared, and short wave infrared portions of the spectrum. Its images has 30 meters multispectral resolutions with a 185 km wide swath, expanse Earth's landscape to offer sufficient resolution to separate features as farms, forests, urbans etc. (Table 5.2).

Table 5.2 : OLI system specifications [18].

Features	Parameters
Sensor Type	Push Broom
Spatial Resolution	30m (15m PAN)
Spectral Range	0.43 – 1.39 μm
Temporal Resolution	16 Days
Image Size	185 km × 180 km
Swath	185 km
Programmable	Yes

The TIRS is a pushbroom sensor and utilizes QWIP (Quantum Well Infrared Photodetectors) which is used for measuring the thermal energy emitted by the surface of Earth (Table 5.3). The QWIP is fundamental for thermal infrared bands that permits to seperate the temperature of the atmosphere from Earth's surface temperature. These photodetectors take advantage of complex principles of quantum mechanics [18].

Table 5.3 : TIRS system specifications [18].

Features	Parameters
Sensor Type	Push Broom
Spatial Resolution	100 m
Spectral Range	10.6 – 12.5 μm
Temporal Resolution	16 Days
Image Size	185 km × 180 km
Swath	185 km
Programmable	Yes

Table 5.4 shows the Landsat 8 band features.

Table 5.4 : Landsat 8 bands and their characteristics [16].

Spectral Bands	Wavelength (μm)	Resolution (m)
Band 1 – Ultra Blue	0.43-0.45	30
Band 2 – Blue	0.45-0.51	30
Band 3 – Green	0.53-0.59	30
Band 4 – Red	0.64-0.67	30
Band 5 – Near Infrared (NIR)	0.85-0.88	30
Band 6 – Shortwave Infrared (SWIR) 1	1.57-1.65	30
Band 7 – Shortwave Infrared (SWIR) 2	2.11-2.29	30
Band 8 – Panchromatic	0.50-0.68	15
Band 9 – Cirrus	1.36-1.38	30
Band 10 – Thermal Infrared 1 (TIRS)	10.60-11.19	100 * (30)
Band 11 – Thermal Infrared 2 (TIRS)	11.50-12.51	100 * (30)

5.2 The Copernicus Program

The Copernicus (previously known as GMES) is an European Earth observation program which is governed by the European Commision with the partnership of European Space Agency (ESA). The program is focalized on six topics which are climate change, land, atmosphere, marine, management, security, and emergency. Copernicus program started firstly with an ordinance called as the Baveno Manifesto in May 19, 1998.

The Copernicus program has a wide range of application area such as agriculture, forestry, climate change, urban planning, and fisheries etc. [19]. Seven satellites were launched to space from 1998 to 2018 (Table 5.5).

Table 5.5 : Characteristics of Copernicus missions [20].

Satellite	Launch Date	Sensors	Orbit Height (km)
Sentinel-1A	April 3, 2014	C-SAR	693
Sentinel-1B	April 25, 2016	C-SAR	693
Sentinel-2A	June 22, 2015	MSI	786
Sentinel-2B	March 7, 2017	MSI	786
Sentinel-3A	February 16, 2016	SLSTR, OLCI, SRAL, DORIS, MWR	814
Sentinel-3B	April 25, 2018	SLSTR, OLCI, SRAL, DORIS, MWR	814
Sentinel-5P	October 13, 2017	TROPOMI	824

Ongoing projects of Copernicus program like Sentinel-3, Sentinel-5, and Sentinel-6 will be launched in the following years and the program will be the most succesful Earth observation program all around the world.

5.2.1 Sentinel-2A

Sentinel-2A was launched on June 22, 2015 by Vega rocket in Kourou, French Guiana as one of the Sentinel-2 satellites which are two polar orbiting satellites placed 180° to each other. It covers the Earth's land surface every five days globally. It has a sun-synchronous orbit and its mean altitude is 786 km. The estimated lifespan for Sentinel-2A satellite is 12 years and it was mainly developed by the Airbus Defence & Space Germany and France.

Sentinel-2A satellite is placed with a high resolution MultiSpectral Instrument (MSI) that utilizes a pushbroom concept (Table 5.6). M1, M2, and M3 are the mirror telescopes which sense the reflected solar radiation from the Earth and atmosphere with a 290 km swath width. The incoming radiation beam is split by a filter wtihin in the instrument and focused into two seperate focal plane assemblies which for visible and near infrared and for shortwave infrared bands [21].

Table 5.6 : MSI system specifications [21].

Features	Parameters
Sensor Type	Push Broom
Spatial Resolution	10, 20, 60 m
Spectral Range	0.4 – 2.2 μm
Temporal Resolution	5 Days (by two-satellite constellation)
Image Size	100 km × 100 km
Swath	290 km
Programmable	Yes

It consist of 13 spectral bands that have 10 m, 20 m and 60 m spatial resolution (Table 5.7) [21]. The spatial and spectral resolution differences of Sentinel-2A and Landsat 8 are shown in the Figure 5.3.

Table 5.7 : Sentinel-2A bands and their characteristics [22].

Spectral Bands	Central wavelength (μm)	Resolution (m)
Band 1 – Coastal aerosol	0.443	60
Band 2 – Blue	0.490	10
Band 3 – Green	0.560	10
Band 4 – Red	0.665	10
Band 5 – Vegetation Red Edge	0.705	20
Band 6 – Vegetation Red Edge	0.740	20
Band 7 – Vegetation Red Edge	0.783	20
Band 8 – Near Infrared (NIR)	0.842	10
Band 8A – Vegetation Red Edge	0.865	20
Band 9 – Water Vapour	0.945	60
Band 10 – SWIR - Cirrus	1.375	60
Band 11 – SWIR	1.610	20
Band 12 – SWIR	2.190	20

Sentinel high-resolution twin satellites are mainly designed for the data continuity and enhancement of Landsat and SPOT type missions and its applications are mostly focused on land cover/use change detection, risk mapping, fast images for disasters, and geophysical maps such as leaf area index, plant chlorophyll and water content [22].
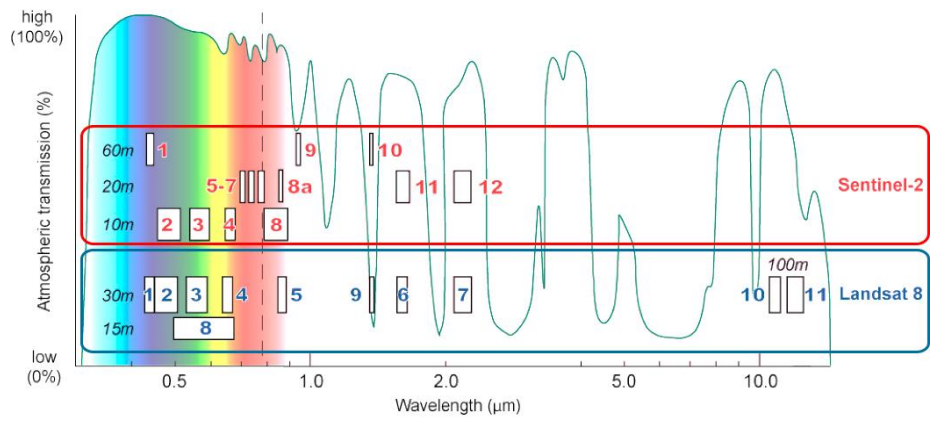
Figure 5.3 : Spatial and spectral resolution differences between Sentinel-2A and Landsat 8 satellites.

6. DIGITAL IMAGE PROCESSING

6.1 Digital Image

Basically, because of the word digital means that information can be displayed electronically on a computer screen, digital image is defined as a two-dimensional image that can be simply processed with the help of computer. In other words, digital image is a numerical transformation of the received radiances by the remote sensing sensor, which is a representation of two-dimensional (2D) matrix of numbers (also three-dimensional (3D) with the spectral dimension) [1, 35].

Computers can just process arrays of digital numbers; on the other hand, they cannot manipulate continous images. Therefore, it is essential to represent images as 2D arrays of points. A individual point on 2D image is known as pixel ("Picture Element"). A pixel indicates the irriadiance at the equivalent grid position. Furthermore, the brightness value of a pixel is called digital number (DN). Figure 6.1 demontrates the representation of digital images [1, 36].
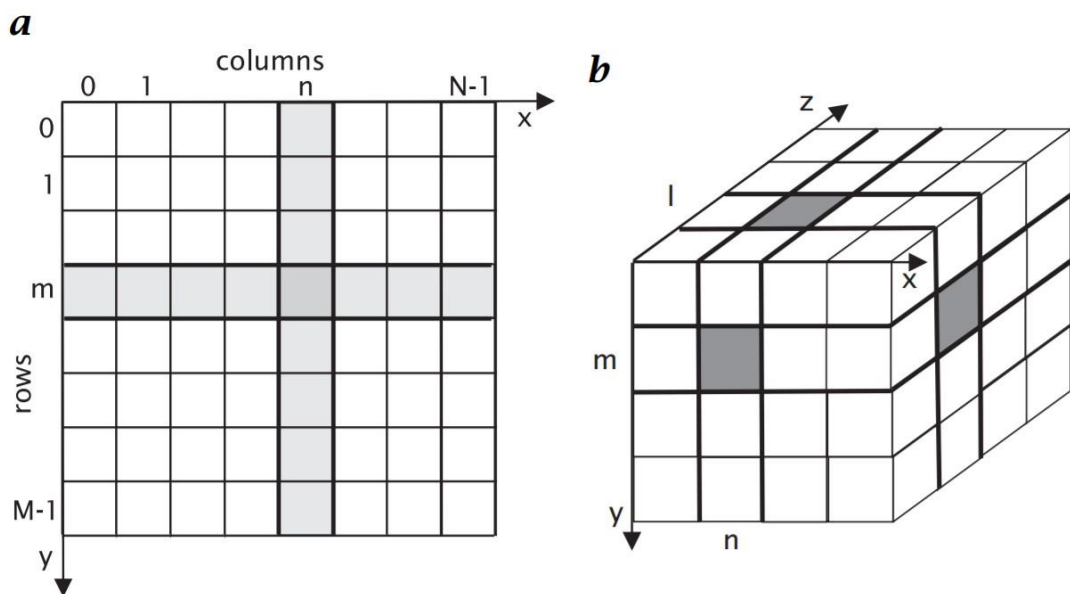

Figure 6.1 : Representation of digital images: (a) 2D image, (b) 3D image [36].

The matrix notation includes the pixel position. The index m, specifies the row position, the second index n, indicates the columns position. If an digital image is M x N dimension which is represented by an M x N matrix, where M is the number of rows and N is the number of columns, so n can obtain values from 0 to $N-1$, and m from 0 to $M-1$ [36].

Eventually, extracting, transmitting, and storage the information of a digital image is inexpensive. Therefore, analyzing, modelling, and displaying the remotely sensed digital data is the simplest and most effective way.

6.2 Resolution

Elementarily, the shortest distance between two surface objects which can be recognized on the image is defined as resolution. If these objects are closer than the resolution, it will be seem as a single object. In addition, the term resolution in remote sensing is utilised as the resolving power, and it is not only the ability to identify the minimum distance of two objects but also their characteristics. Actually, the term resolution is the quantity of details which can be monitored on the image in a qualitative meaning. To characterise a image as fine resolution, the image have to demonstrate finer details than coarser details [37]. Four types of resolutions are defined for the remote sensing systems; spatial resolution, spectral resolution, radiometric resolution, temporal resolution [1].

- Spatial Resolution: The capability of measuring the smallest object on the image is defined as the spatial resolution. Depending on the camera focal length and height above the ground, spatial resolution specifies the minimum discrimination of objects that how independent and isolated they are.

- Spectral Resolution: It identified the number of bands which is supplied by the remote sensing sensor, and also their spectral bandwiths. In more detail, discrimination capacity of the sensor depends on band number, the capacity will increase with the rise of the number of band.

- Temporal Resolution: The frequency of acquisition of the remotely sensed image by the sensor of a area of interest. It mainly depends on orbital properties such as height, and declination etc.

- Radiometric Resolution: The discrimination of small differences in the magnitude of radiation is defined as the radiometric resolution. It is determined by the number of bits. For example, a data with 8 bit will range the brightness values between 0 and 255 for each pixel ($2^8 = 256$).

6.3 Image Processing

Basically, image procesing is defined as the technology that involves many different processing steps on an image in order to obtain a better image or to extract useful information from the image [35]. These processing steps are generally consist of three different steps which are pre-processing, image enhancement, and classification.

6.3.1 Pre-processing

The pre-processing is a fundamental step for remotely sensed data which performs calibrations and eliminates the systematic errors. The principal applications of pre-processing are the radiometric and geometric corrections [6].

The radiometric calibration is hard and extraordinary for photographic imagery but it needs to be calibrated occasionally. There are two efficient steps in optical and infrared systems for radiometric calibration. Firstly, the relevance between the value of the pixel recorded by the sensor and spectral radiance is builded. In other words, pixel values are transformed to radiance values. In the second step, the atmospheric propagation effects are eliminated for acquiring the surface radiances. Because of the different type of illumination of obtained optical imagery, the impact of the illumination geometry is corrected. In addition, instruments have internal calibrators which calibrate itself periodically [6].

Maps are representations of the Earth, which are projected onto a planar base according to certain mathematical cartographic and geodetic projection rules and have uniform scale at each point. Digital images cannot be used directly as a map because of geometric distortions originating from several reasons. In other words, the distances between the geographical areas represented by the pixels forming the image are displayed incorrectly in a non-uniform manner. As a result, the features such as shape, size and position of the objects are distorted in the image plane. The process of correcting satellite image data for these distortions and making them consistent with a

map projection is called rectification [7]. The following steps describe the geometric correction process [38]:

- Selecting the convenient reference map or image.

- Selecting a regular grid that is suitable for the convenient projection.

- Selecting a number of ground control points (GCP).

- Identifying the transformatiom, and calculating the locations of the grid points on the coordinate system of the output image.

- Assigning the gray scale values of each grid point by resampling in the output image.

6.3.2 Spectral transformations

Digital image enhancement is the process of changing the information content in the image to achieve more effective results in a particular application. The type and effectiveness of the methods depending on the application area, and differ from image to image to be used [35].

Spectral transformations are image enhancement methods that are applied to the image in the spatial domain, in other words at the level of pixel brightness values (gray scale). In contrast to spatial transformations, spectral transformations are applied independently on each pixel without any neighborgood information. Examples of spectral transformations are histogram transformations, arithmetic transformaitons, and Principal component analysis (PCA). Image statistics such as average, variance, and coveriance are used intensively to apply these methods. The variables that enter the algorithms are called features. Any information of pixels can be features; but the feature space which is a cluster that are composed of different valid features of each pixel, is usually generated by pixel brightness values [35].

6.3.2.1 Spectral burn indexes

The brightness values of multiple bands can be used in mathematical algorithms, and the information about target features can be revealed, isolated and analysed. In this context, spectral burn indexes are frequently used as an effective method to show the optimum impacts of the fire. Because of their cognitive simplicity and computational performance, spectral burn indexes are largely used as spectral transformation

technique. Burn indexes discriminate the post and pre-fire images; therefore, they seperate the burned area from other surface features such as water, dark soil or mining sites by the use of their spectral curves [39, 41]. The mathematical formulas of spectral burn indexes (Burn Area Index (BAI), Normalized Burn Ratio (NBR) and Normalized Burn Ratio – Thermal (NBRT) and Mid-Infrared Burn Index (MIRBI)) are given below [39, 40, 41].

The Burn Area Index (BAI):

$$BAI = \frac{1}{(0.1 - Red)^2 + (0.06 - NIR)^2} \tag{6.1}$$

The Burn Area Index (BAI) is utilised particularly for the detection and enhancement of the burned (char) signal. The BAI computes the spectral distance from each pixel to the combination of burned pixels that is a reference point by the use of red and NIR bands. The reference (spectral) values 0.1 and 0.06 are calculated from a number of satellite sensor images [41].

The Normalized Burn Ratio (NBR):

$$NBR = \frac{(NIR - SWIR)}{(NIR + SWIR)} \tag{6.2}$$

The Normalized Burn Ration (NBR) is specifically designed for extracting the burned areas, and also determine the burn severity. It uses the Near Infrared (NIR) and Shortwave Infrared (SWIR) bands different from the NDVI (Instead of SWIR, NDVI uses Red band). It is known that healthy vegetation has a high NIR reflectance and low SWIR reflectance in the EM spectrum. However, burned areas have low reflectance in NIR and high reflectance in SWIR bands [41] (Figure 6.1).
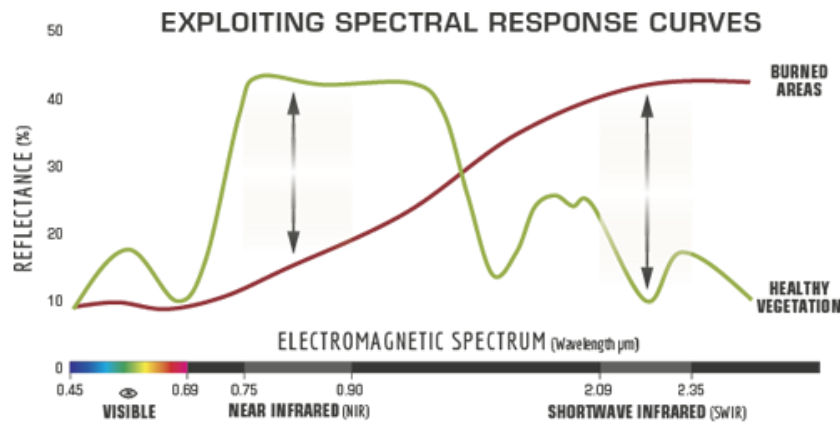

Figure 6.2 : Spectral curves of healthy vegetation and burned areas (©US Forest Service).

The Normalized Burn Ratio – Thermal (NBRT):

$$NBRT = \frac{\left(NIR - SWIR\left(\frac{THERMAL}{1000}\right)\right)}{\left(NIR + SWIR\left(\frac{THERMAL}{1000}\right)\right)} \qquad (6.3)$$

Different from NBR, NBRT is normalized with the thermal band to enhance the post-fire changes.

The Mid-Infrared Burn Index (MIRBI):

$$MIRBI = 10LSWIR - 9.8SSWIR + 2 \qquad (6.4)$$

The MIRBI was specially created for savannah ecosystems because the use of NIR bands are unnecessary in that type of vegetations.

The NBR is also fundamental for estimating the burn severity. Burn severity is the quantification of the magnitude of ecological alteration due to the forest fire. NBR is used to measure and map this burn severity quantitatively and qualitatively [39]. The post-fire NBR dataset is discriminated from pre-fire NBR dataset to generate a scaled index (dNBR) of the burn severity. This index (dNBR) is compatible with land measurements especially in the Mediterranean forest areas [33]. Following equation (6.5) states the mathematical algorithm of dNBR index.

$$dNBR = NBR_{pre-fire} - NBR_{post-fire} \qquad (6.5)$$

NBR index values vary theoretically from -1 to +1, whereas dNBR values can vary from -2 to + 2. The Table 6.1 provided by the US Geological Survey (USGS) is used for determining the levels of burn severity.

Table 6.1 : Levels of burn severity (©USGS).

dNBR	Burn Severity
< -0.25	High post-fire regrowth
-0.25 – -0.1	Low post-fire regrowth
-0.1 – +0.1	Unburned
0.1 – 0.27	Low-severity burn
0.27 – 0.44	Moderate-low severity burn
0.44 – 0.66	Moderate-high severity burn
> 0.66	High-severity burn

6.3.3 Land surface temperature determination

Thermal infrared (TIR) imagery techniques based on the principle of all objects emit energy having temperature above absolute zero are used to determine the land surface temperature (LST). Thermal sensing systems measure the thermal energy based on the kinetic temperatures of the objects and the radiated temperature according to the surface emissivity (ε) values [7]. Many algorithms have been developed to determine the LST such as mono-window, split-window, single channel, temperature-emissivity separation, and the land surface temperature algorithm.

The land surface temperature algorithm which is customised for Landsat 8 involves these following stages for computing the LST [18, 42].

- Transformation of digital numbers (DN) to spectral radiance values.

- Transformation of spectral radiance values to brightness temperature values.

- Computing the surface emissivity (ε) values.

- Finally, calculating the land surface temperature.

First of all, equation (6.6) is used to convert the digital numbers (DN) to the spectral radiance values, and equation (6.7) is used to calculate the brightness temperature values.

$$L_\lambda = M_L \times Q_{cal} + A_L \tag{6.6}$$

$L_\lambda =$ spectral radiance (W/(m2 * sr * μm)).

$M_L =$ band-specific multiplicative rescaling factor from the metadata.

$A_L =$ band-specific additive rescaling factor from the metadata.

$Q_{cal} =$ L1 pixel value as digital number.

$$T = \frac{K2}{\ln\left(\frac{K1}{L_\lambda}+1\right)} \tag{6.7}$$

$T =$ brightness temperature (K).

$K1 =$ band-specific thermal conversion constant from the metadata.

$K2 =$ band-specific thermal conversion constant from the metadata.

Normalized Difference Vegetation Index (NDVI) (equation (6.8)) is used to calculate the surface emissivity (ε) values.

$$NDVI = \frac{NIR - Red}{NIR + Red} \qquad (6.8)$$

If NDVI < 0.2 then the pixel values are considered as bare soil and emissivity is computed as 0.97.

If NDVI > 0.5 then the pixel values are mostly vegetation and the emissivity value is 0.99.

If $0.2 \leq$ NDVI ≤ 0.5, then the pixel values are combination of bare soil and vegetation and the emissivity is calculated in the following equation (6.9) [42].

$$\varepsilon = \varepsilon_v \times P_v + \varepsilon_s \times (1 - P_v) + d\varepsilon \qquad (6.9)$$

ε_v is vegetation emissivity.

ε_s is soil emissivity.

P_v is vegetation proportion calculated according to equation (6.10) [42].

$$P_v = \left(\frac{NDVI - NDVI_{min}}{NDVI_{max} + NDVI_{min}}\right)^2 \qquad (6.10)$$

Consequently, the LST is computed according to the emissivity values as follows (equation (6.11)) [42].

$$LST = \frac{T}{1 + \left(\frac{\lambda \times T}{\rho}\right) \times \ln(\varepsilon)} \qquad (6.11)$$

λ is the central band wavelength of emitted energy.

$\rho = h*c/\sigma$ (1.438 x 10^{-2} m x K).

h is the Planck constant (6.626 x 10^{-34} J*s).

σ is the Boltzmann constant (1.38 x 10^{-23} J/K).

6.3.4 Image classification

Image classification is the process of identifying meaningful pattern groups in the image that constitute thematic information. In other words, image data with different spatial, spectral, radiometric and temporal components are transformed into descriptive labels or thematic information that categorize different surface materials and conditions. With the classification process, quantitative decision functions are

created to determine and identify different characteristics or objects in the image. Spectral and spatial information based on the image and other ancillary data depending to the region are used in the creation of quantitative decision functions. Feature is the information which will be the input for the classification process, and feature space is the space created by these features [7]. Figure 6.2 shows the principle of classification of remotely sensed data.
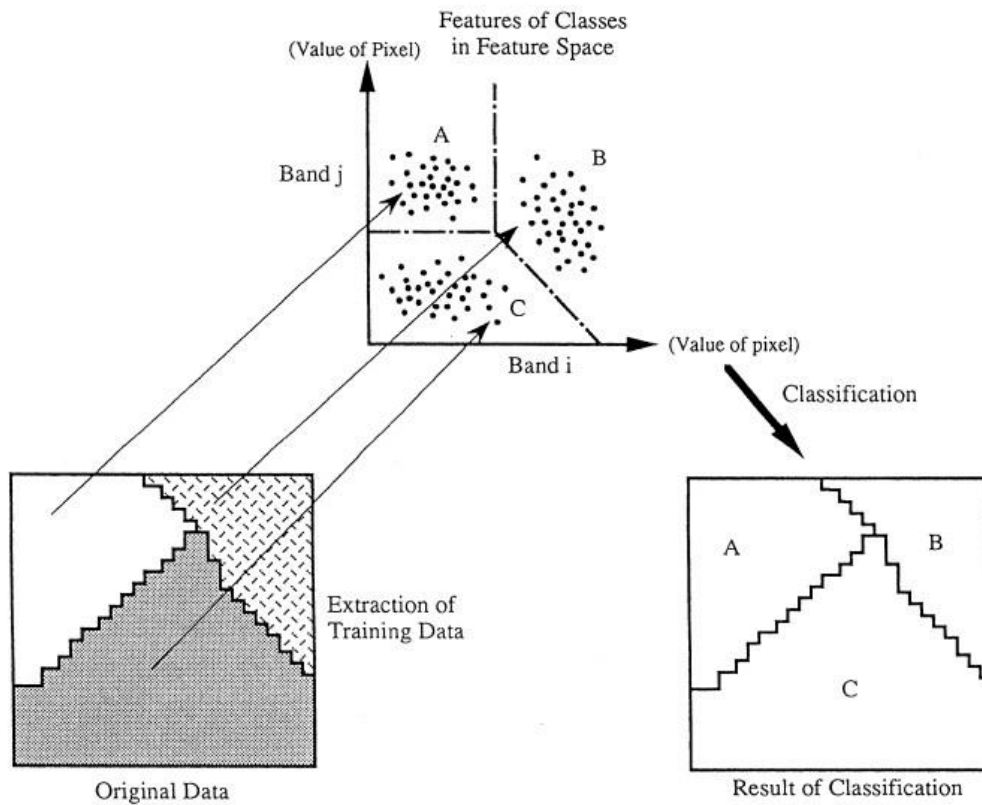

Figure 6.3 : Principle of classification of remotely sensed data [43].

6.3.4.1 Unsupervised classification

The main purpose of the unsupervised classification, in which no apriori thematic information is used, is to reveal natural groups (clusters) that provide a certain criterion in the feature space. Patterns with similar feature vectors form a group of points in a cloudlike view. Each group specifies a multi-dimensional representation for patterns of a different object category. The resultant clusters are not known as which categories they refer, but the class responses of clusters are known through field measurements, maps and aerial photographs.

ISODATA (Iterative self-organizing data analysis) algorithm is one of the most used unsupervised classification methods. In this method, a lower limit for the number of

pixels of clusters which are formed and an upper limit depending on a certain standard deviation value can be determined. Accordingly, the number of classes may result in more or less than the desired number as a result of clustering. In addition, not only the number of iterations but also the rate of variation between the iterations can be used to terminate the process [7].

6.3.4.2 Supervised classification

Basically, supervised classification algorithms demonstrating the representative spectral values of each land cover property by knowing the sample cover types. All the sample regions are called training areas, and the representative values are also known as spectral signatures. After determining the spectral signatures of the land cover types, classification process is terminated. Each pixel value is estimated or classified based on the resemblance to the representative spectral signatures. There are different supervised classification methods such as Maximum Likelihood, and Support Vector Machine algorithms.

In the Maximum Likelihood method, a pixel is assigned to the class that has the highest probability value. A probability distribution model is needed to calculate these probabilities. Accordingly, it is assumed that each class of training data has a Normal (Gaussian) distribution. In fact, although this assumption is not true, it has been observed that normal distribution is appropriate and classification algorithms based on this acceptance are stronger algorithms in the modeling of optical remote sensing data [7].

Support Vector Machines are an efficient statistical classification method that determines how to define the boundary line (hyperplane) that can best distinguish two or more classes from each other. The way the boundary line is defined depends on the training data used for the classification and the characteristics of the classes to be considered. The main problem is that the linear boundary determination for the dataset can be created in infinite different ways. The Support Vector Machines method selects the most appropriate linear boundary by trying to maximize the success of classification according to certain criterions between these infinite number of linear boundary definitions [35].

6.3.4.3 Classification accuracy

The concept of accuracy in classification refers to the assignment of patterns to the categories to which they really belong. Assignment of patterns to incorrect classes is a classification error. Therefore, the smaller the error, the higher the accuracy. The accuracy criteria used in the applications are empirical values because it is not known which categories the pixels actually refer. In other words, they are estimated statistical values of the theoretical parameters. The most common approach is to use the training dataset which calculates the decision functions required to assign the patterns to categories in determining the degree of accuracy. However, this approach is statistically biased. Accordingly, a new neutral dataset called test data must be created that is different from the training dataset but represents the same classes [7].

The most common approach for determining the accuracy of classification is the use of error matrix. Reference data (test data) that are considered to refer to all relevant categories are used in the creation of the error matrix. In the applications, the most commonly used accuracy criterion for classification is the overall accuracy. The following equation (6.12) identifes the overall accuracy formula [7].

$$Overall\ accuracy = \frac{\sum_{i=1}^{k} n_{ii}}{n} \tag{6.12}$$

k is the number of classes.

n is the total reference data number.

i is the number of rows of the error matrix.

Equation (6.13) and (6.14) state the Producer and User accuracies respectively which avoid biased accuracy [7].

$$Producer\ accuracy = \frac{n_{jj}}{n_{+j}} \tag{6.13}$$

j is the number of columns of the error matrix.

$$User\ accuracy = \frac{n_{ii}}{n_{i+}} \tag{6.14}$$

7. APPLICATION & RESULTS

The aim of this projcet is to analyse the environmental changes and effects of the forest fire occured in Menderes region of Izmir with the integration of remote sensing pre-fire and post-fire satellite maps, and GIS data created from a field work and forest management plans.

7.1 Study Area and Data Used

The forest fire took place in the Menderes district which is within the border of Izmir Forestry Chief Directorate located in the Aegean region of Turkey (Figure 7.1). The fire started on July 1, 2017 in maquis forest area and continued for 4 days, and extinguished on July 5, 2017.

Figure 7.1 : Google Earth view of the study area.

Menderes region is mostly covered with Calabrian pine (*Pinus brutia*) tree species and the elevation of the region varies between 90 m and 450 m. Moreover, the slope is between 5 and 65 %. Meteorological data (mean and maximum wind velocity, wind direction, mean relative humidity (%), mean air temperature (°C), mean atmospheric

pressure) were acquired from the Menderes meteorological station close to the fire region. According to this data, the average temperature of the region was 35°C on July 1, 2017 and the maximum temperature reached to 42°C (Figure 7.2). During the fire (July 1, 2017) the wind was blowing from the North and Northeast and the average wind speed was measured as 7 m/s.
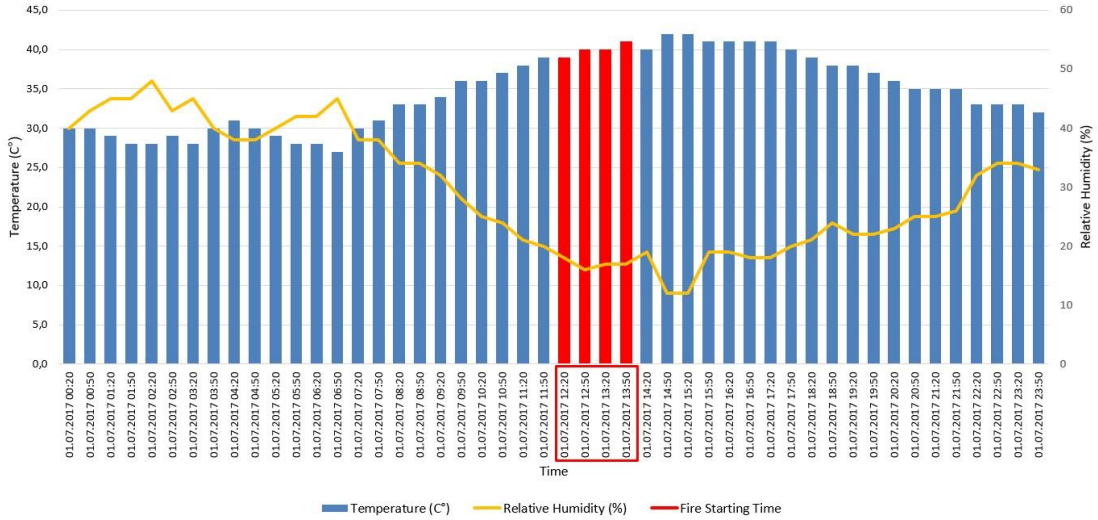

Figure 7.2 : Air temperature and relative humidity of Menderes on July 1, 2017 (Meteorological Service, 2018).

It is thought that the high air temperature and wind speed in the region affected the forest fire in the Menderes region of Izmir (Table 7.1). In general, wind with a speed between 3 and 9 m/s is known to cause large forest fires [44]. The average relative humidity during the fire was 30 %.

Table 7.1 : Meteorological parameters effecting a forest fire [44].

Parameters	Optimum Values	Average values in Menderes
Temperature	> 25°C	35°C
Wind Speed	3 – 8,8 m/s	7 m/s
Relative Humidity	< 40%	30%

Before the fire in June 2017, the mean weather temperature was 25.6 °C and the mean realtive humidity was 42.1 %.

Menderes forest area consists of a partly rocky area. These areas were also affected by the fire, but they were not included in the burned region as they were not considered as forest area (Figure 7.3).
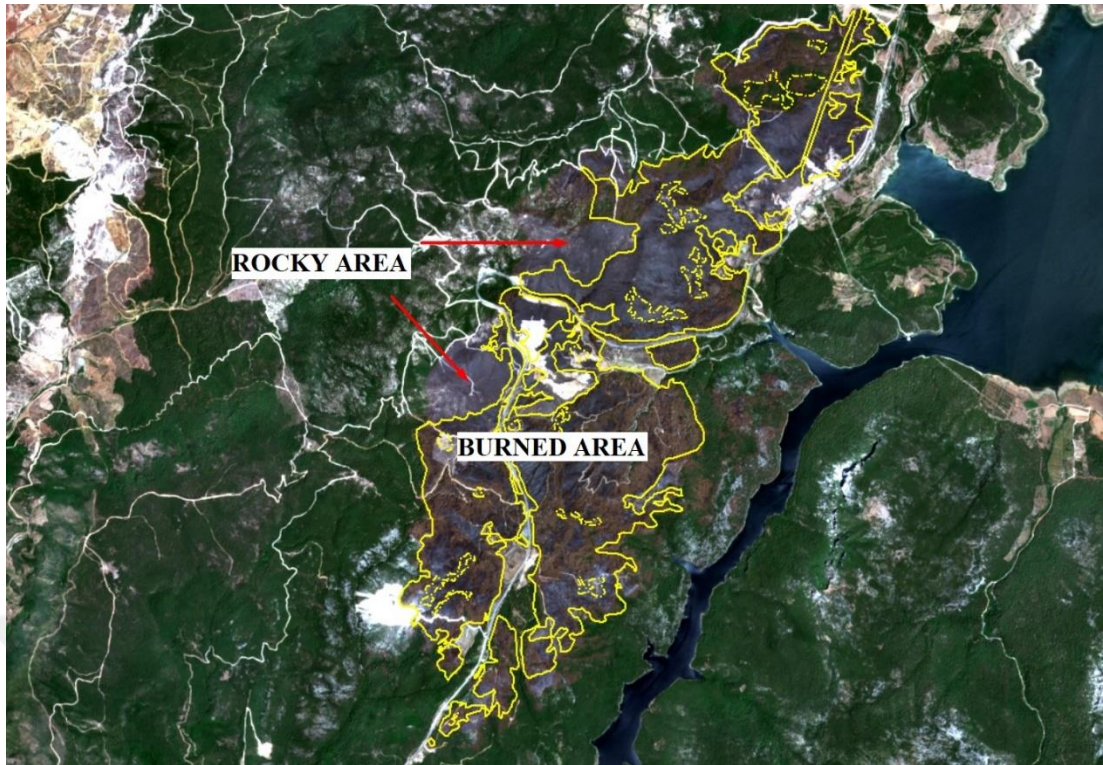
Figure 7.3 : Burned and rocky areas in Menderes.

For this study, cloud-free Landsat 8 satellite images acquired before (30 June 2017) and after (16 July 2017 and 3 July 2018) the fire, and Sentinel 2 image acquired after (22 July 2017) the fire were used. For classification of Landsat 8 satellite images, the bands between 2 and 7 with a spatial resolution of 30 m were used. TIRS thermal bands 10 and 11 which have 100 m spatial resolution were used to estimate the land surface temperature of Landsat 8 images. For classification of Sentinel 2 satellite image, the bands 2, 3, 4, and 8 with a spatial resolution of 10 m were used. These bands were sampled to 20 m spatial resolution and utilised with other bands (5, 6, 7, and 8a) which have 20 m spatial resolution to evaluate the efficiency of the spatial resolution on classification accuracy. Figure 7.5 and Figure 7.6 show the natural color images of the study area.

A GIS data generated by the Izmir Foresty Chief Directorate were also utilised, which demonstrating the slope, vegetation type, and canopy density in Menderes region, for intergrating it with the remote sensing data.

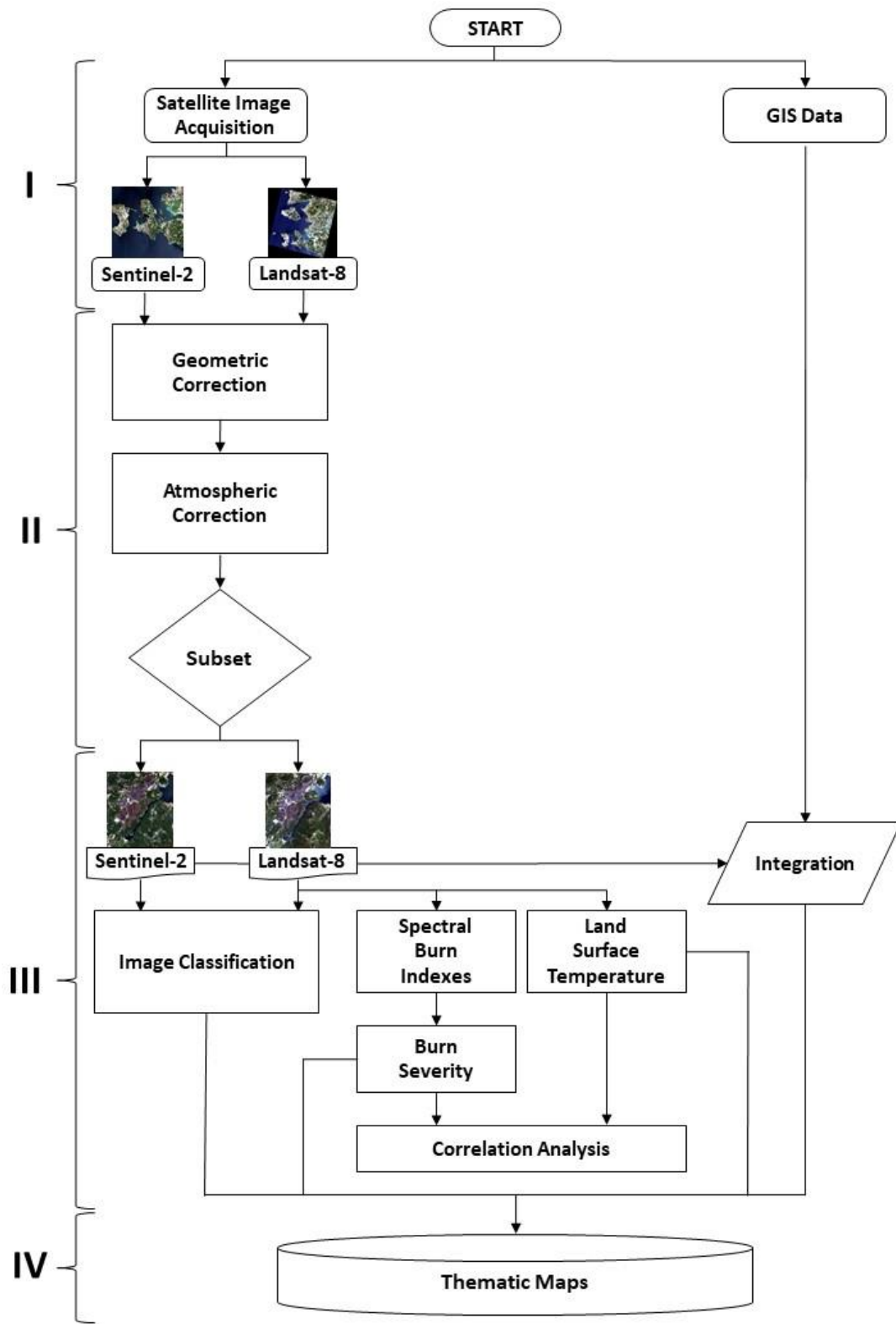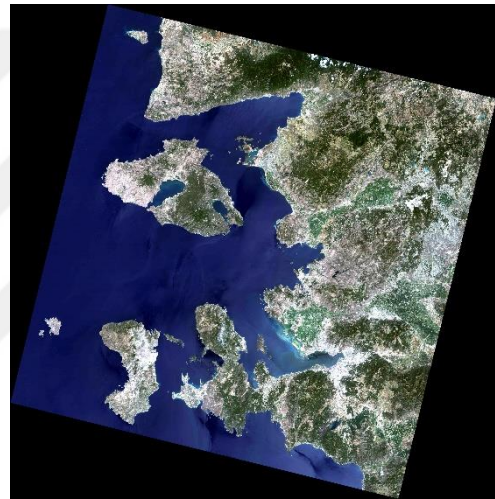Figure 7.4 shows the flow chart of the study.
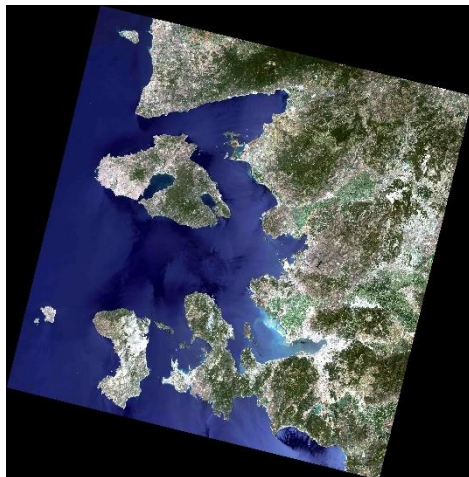
Figure 7.4 : Flow chart of the study.

Figure 7.5 : Sentinel 2 natural colour image dated 22.07.17.

(a)

(b)

(c)

Figure 7.6 : Landsat 8 natural colour images dated. (a) 30.06.17 (b) 16.07.17 (c) 03.07.18

7.2 Geometric Correction

Landsat 8 images are georefenced on Universal Transverse Mercator (UTM) coordinate system, WGS-84 datum. However, Sentinel 2 satellite image is not georeferenced on any coordinate system; therefore, Landsat 8 images were used as map and Sentinel 2 image was registered to Landsat image using rectification process.

First of all the Ground Control Points (GCPs) were selected and marked on Sentinel 2 image as demonstrated in Figure 7.7.
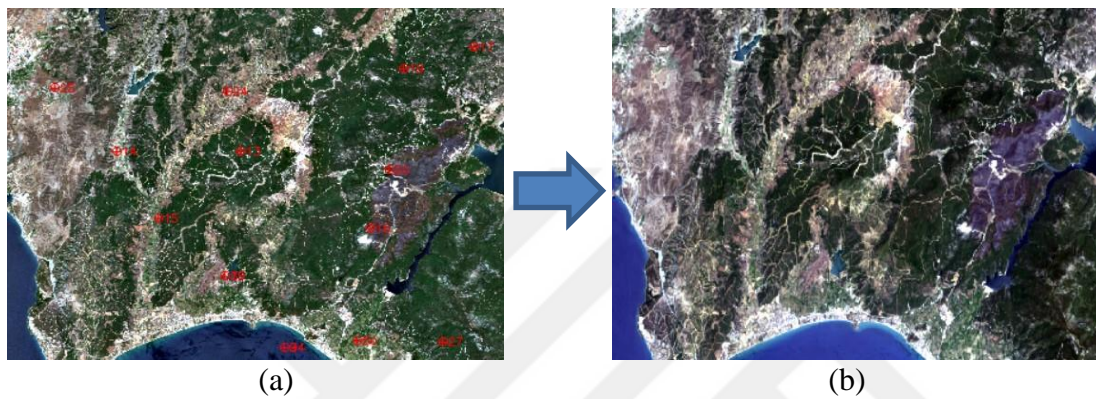

(a)   (b)

Figure 7.7 : Image to map registration. (a) Sentinel 2 (b) Landsat 8

The Sentinel 2 satellite image dated July 22, 2017 was georeferenced with ± 0.26 rms (Root Mean Square) error. Figure 7.8 shows the georeferenced and subsetted Sentinel 2 satellite image. Furthermore, subsetted Landsat 8 images are demonstrated in Figure 7.9.

Figure 7.8 : Georeferenced and subsetted Sentinel 2 image (22.07.2017).

50

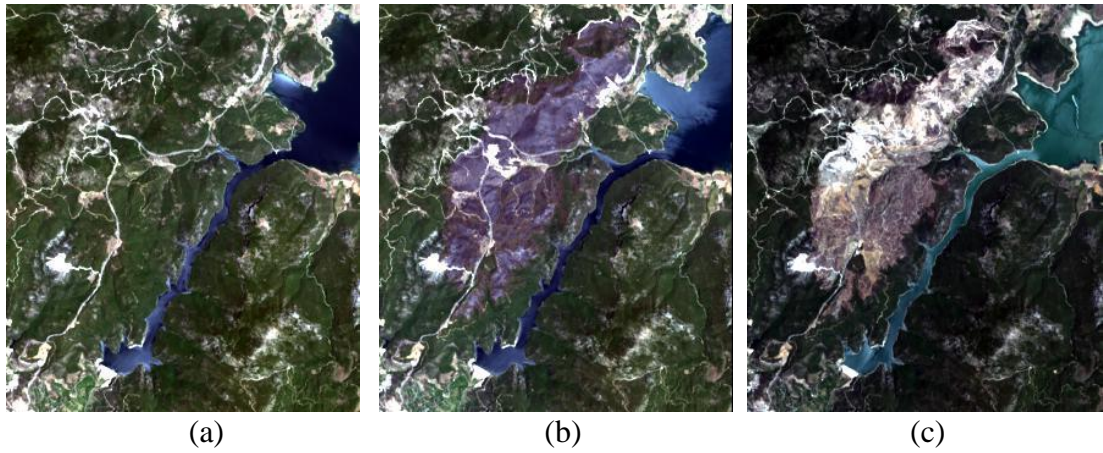(a)   (b)   (c)

Figure 7.9 : Subsetted Landsat 8 images. (a) 30.06.2017 (b) 16.07.2017 (c) 03.07.2018

7.3 Spectral Transformations

As stated previously, spectral transformation which is performed on the image in the spectral domain is an image enhancement method. In this study, spectral burn indexes were applied as a spectal transformation algorithm to measure the environmental changes of the forest fire occured in Menderes, Izmir.

7.3.1 Spectral burn indexes

Several spectral burn indexes are developed to determine a forest fire such as Burn Area Index (BAI), Normalized Burn Ratio (NBR) and Normalized Burn Ratio – Thermal (NBRT) and Mid-Infrared Burn Index (MIRBI). Table 7.2 shows the mathematical formulation of the mentioned burn indexes.

Table 7.2 : Mathematical formulation of the spectral burn indexes used in this study.

Spectral Burn Indexes	Mathematical formulation
Burn Area Index (BAI)	$BAI = \dfrac{1}{(0.1 - Red)^2 + (0.06 - NIR)^2}$
Normalized Burn Ratio (NBR)	$NBR = \dfrac{(NIR - SWIR)}{(NIR + SWIR)}$
Normalized Burn Ratio – Thermal (NBRT)	$NBRT = \dfrac{\left(NIR - SWIR\left(\frac{THERMAL}{1000}\right)\right)}{\left(NIR + SWIR\left(\frac{THERMAL}{1000}\right)\right)}$
Mid-Infrared Burn Index (MIRBI)	$MIRBI = 10LSWIR - 9.8SSWIR + 2$

These spectral burn indexes were applied to July 16, 2017 dated Landsat 8 satellite image (Figure 7.10).

(a)   (b)

(c)   (d)
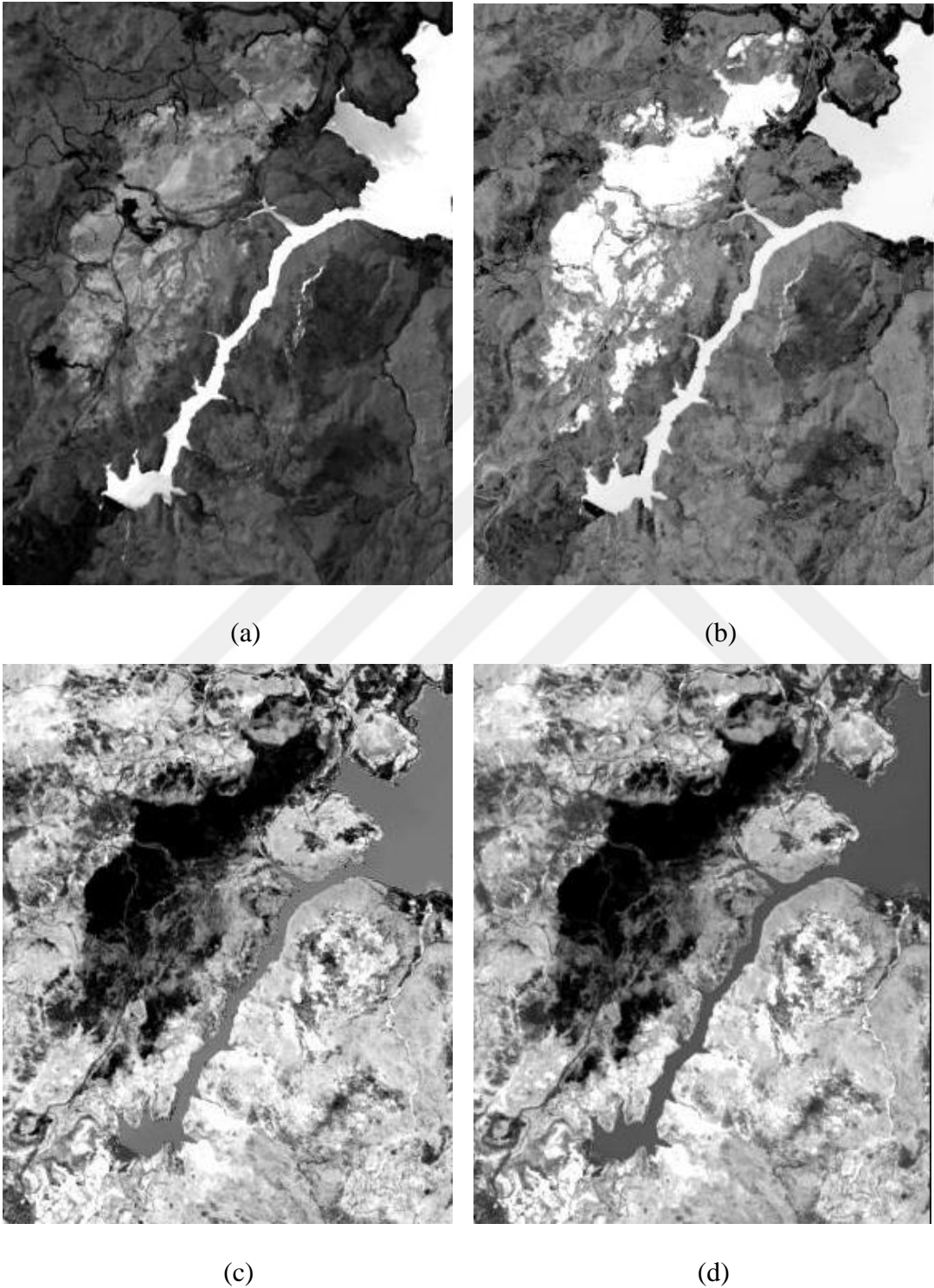
Figure 7.10 : Spectral burn indexes. (a) BAI (b) MIRBI (c) NBR (d) NBRT.

As it is known, the aim of spectral burn indexes are to reveal, isolate, and analyse the target features from the remotely sensed images. The BAI was specifically designed for the determination of the char signal. As seen from Figure 7.10.a, some parts of the forest fire area are mixed with the lake pixels besides the burned area but it achieved to seperate burned areas from unburned areas. The MIRBI was particularly generated for the detection of burned savannah ecosystems. However, the Menderes area is mainly consist of Calabrian pine (*Pinus brutia*) tree species; therefore, it was unsuccesful to seperate burned area from other areas like lake and mine pixels. As demonstrated in Figure 7.10.b, the burned area was mixed with the lake pixels. The purpose of NBR index is to extraxt the burned areas and determine the burn severity. The NBR index was quite successful to extraxt the burned areas as shown in the Figure 7.10.c. The NBRT index was also successful to determine the burned areas (Figure 7.10.d).

The dNBR index was used to determine the burn severity. This index is observed to be compatible with the field measurements made especially in the Mediterranean forest areas; therefore, it has become a widely used index for the evaluation of the burn severity. In order to generate a scaled index (dNBR) of the fire, the NBR dataset of post-fire dated July 16, 2017 is removed from the pre-fire NBR data set dated June 30, 2017. Figure 7.11 shows the burn severity of the forest fire area in the image dated July 16, 2017.
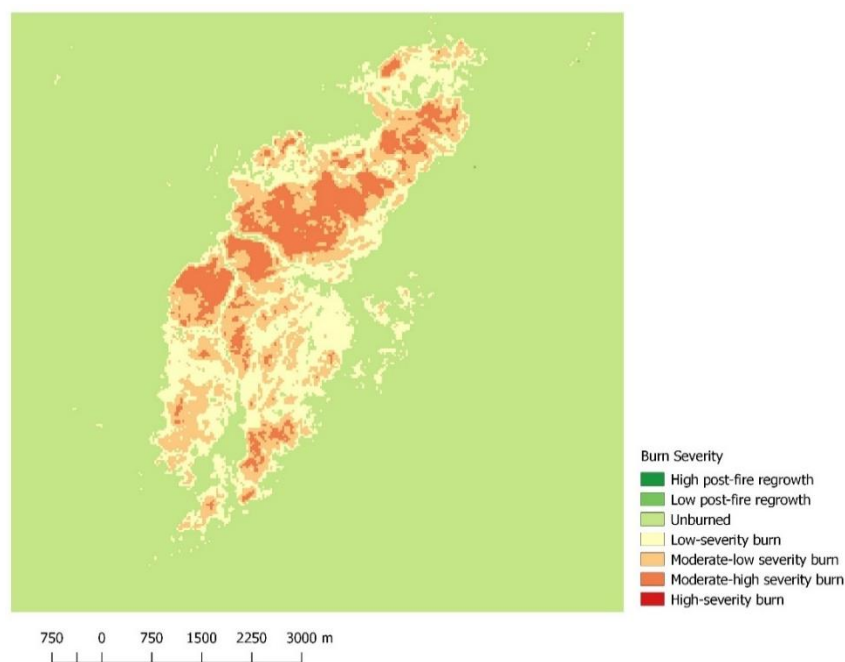

Figure 7.11 : The burn severity of Menderes in the image dated 16.07.2017.

The same process was performed on the Landsat 8 satellite image dated July 3, 2018 (i.e. was acquired one year after the fire occured on July 1, 2017) to monitor the vegetation survival and mortality as dNBR determines also the post-fire regrowth. Accordingly, a rehabilitation and restoration plan can be improved from burn severity maps. Figure 7.12 demonstrates the burn severity of the Landsat 8 image dated July 3, 2018.
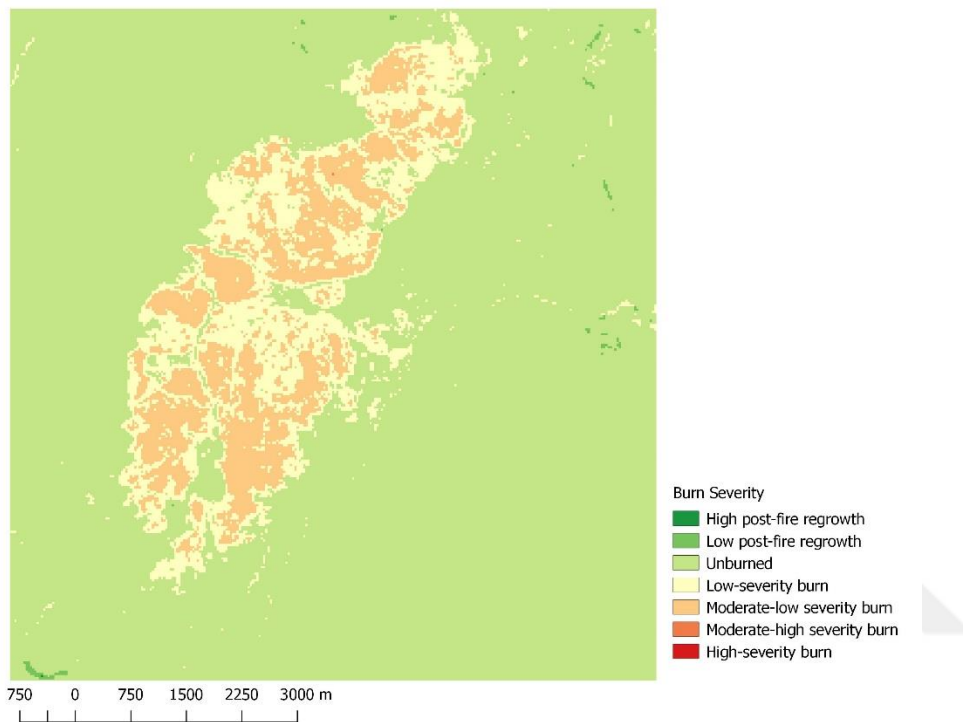

Figure 7.12 : The burn severity of Menderes in the image dated 03.07.2018.

As can be seen from the Figure 7.11, there is no regrowth in the burned forest area even one year after the fire. In this context, it is thought that the majority of trees have died or cut off in a planned way.

7.4 Land Surface Temperature Determination

In this study, Land Surface Temperature (LST) algorithm which is adapted for Landsat 8 was used to determine the land surface temperature. The processing steps performed with this method are; i) converting the digital numbers (DN) to the spectral radiance values, ii) converting the spectral radiance values to the brightness temperature values, iii) calculating the surface emissivity (ε) values, and iv) finally calculating the LST. For this purpose, in order to determine the land surface temperature before and after

the forest fire in the Menderes region, pre-fire (June 30, 2017) and post-fire (July 16, 2017) Landsat 8 satellite images were used.

Firstly, equation (6.6) was used to convert the digital numbers (DN) to spectral radiance values. Afterwards, equation (6.7) was used to calculate the brightness values of the Landsat 8 pre-fire and post-fire satellite images.

For computing the surface emissivity (ε) values, NDVI was used. As it is known, NDVI index values vary between -1 and +1. High NDVI values (where the index values approaches to +1) correspond to green vegetation areas; on the other hand, low NDVI values (where the index values approaches to -1) mean that the area is covered with water, snow, sand, or barren rock.

The P_v (proportion of vegetation) was calculated from equation (6.10) by the use of NDVI values since the pixel values of the study area are mixture of vegetation and bare soil, where the $NDVI_{min}$ is 0.2 and the $NDVI_{max}$ is 0.5. Furthermore, the final equation of surface emissivity (ε) is as follows (equation (7.1)).

$$\varepsilon = 0.004 \times P_v + 0.986 \tag{7.1}$$

Surface emissivity (ε) which is an important parameter in the calculation of the temperature of the bodies is defined as the ratio of the incoming energy beam to the absorbed energy beam. Moreover, the surface emissivity (ε) values are range from 0 to 1. The emissivity values of the objects depend according to the wavelength of the emitted radiation and the geometric position of the objects.

Finally, the corrected land surface temperature values were determined from the equation (6.11) by the use of the surface emissivity (ε) values.

In order to determine the surface temperature change (dLST) of pre-fire and post-fire of the Menderes region, the difference of the two surface temperature images was computed (equation (7.2)).

$$dLST = LST_i - LST_j \tag{7.2}$$

Where *dLST* is the land surface temperature difference, LST_i is the July 16, 2017 dated post-fire image, and LST_j is the June 30, 2017 dated pre-fire image.

Figure 7.13 demonstrates the pre-fire LST and post-fire LST of Menderes, Izmir.

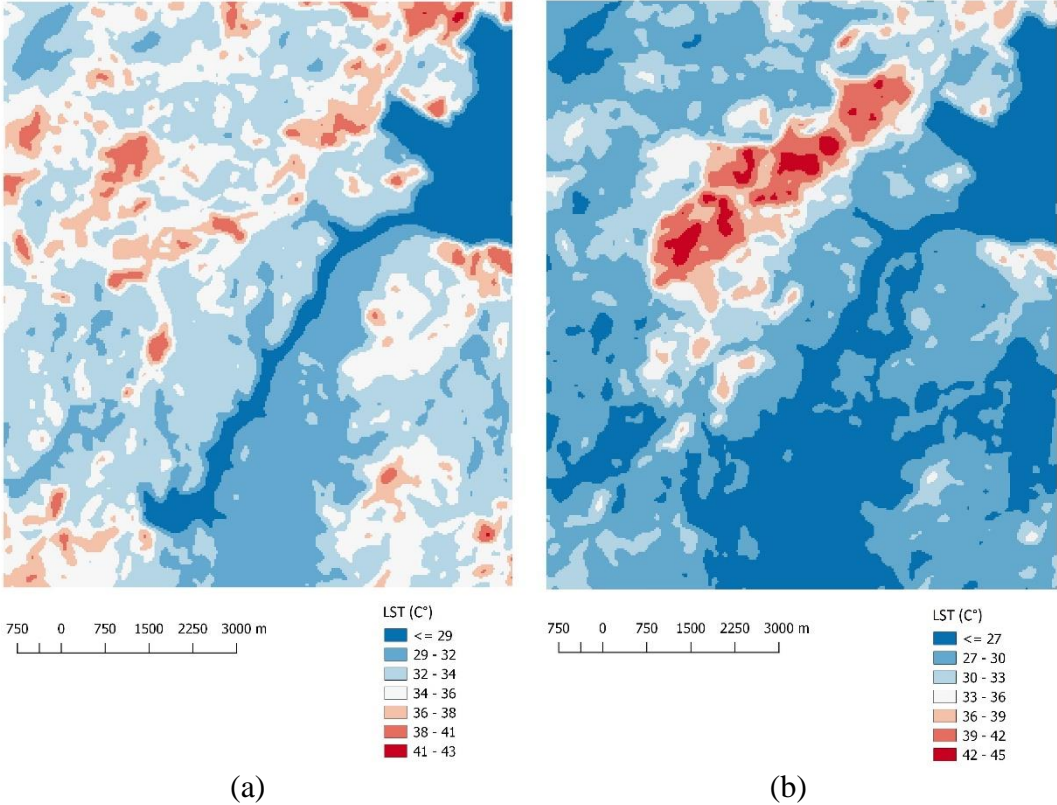(a)   (b)

Figure 7.13 : Land Surface Temperature (LST) maps of Menderes region. (a) 30.06.2017 (b) 16.07.2017

Figure 7.14 shows the dLST of the Menderes region. The LST values of July 16, 2017 dated post-fire image are mapped between 34 – 45 C° by density slicing in the Figure 7.15.
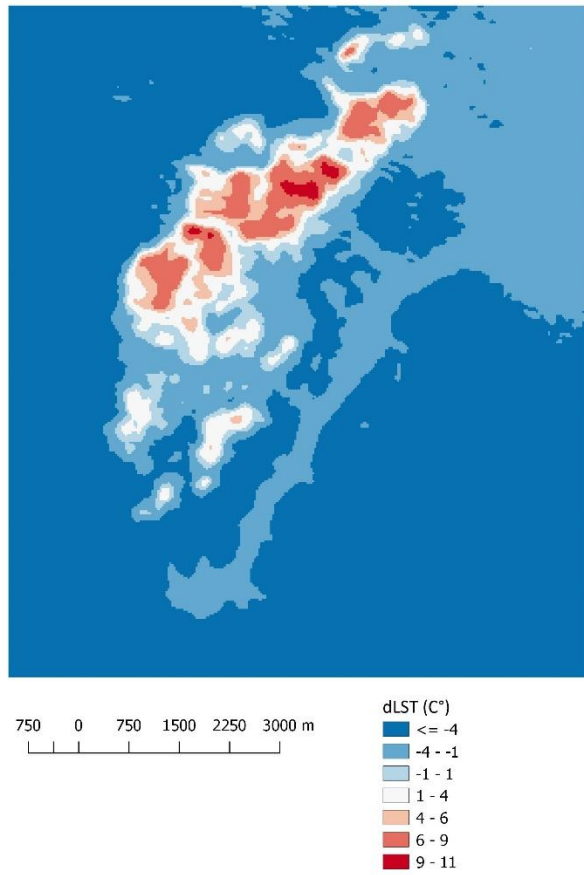
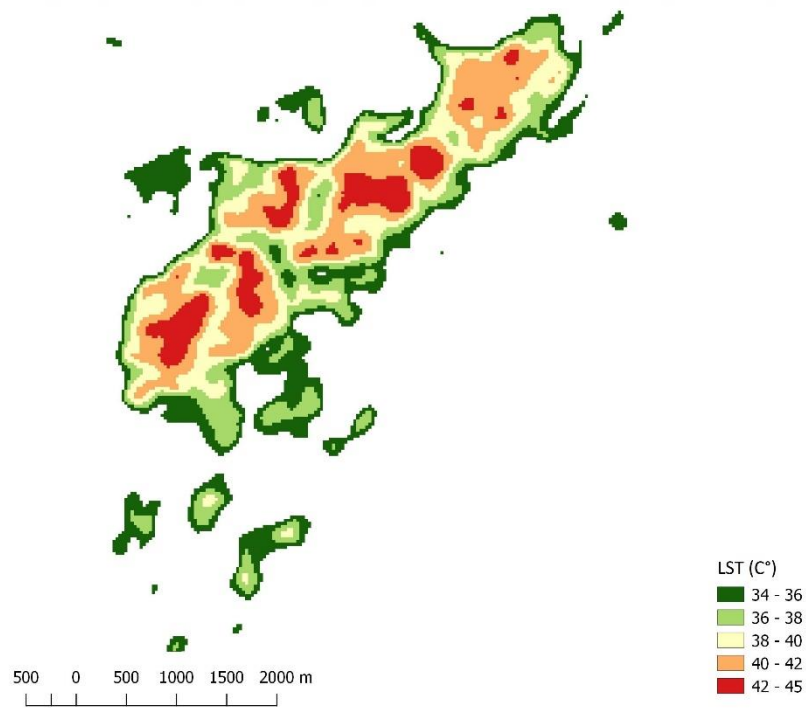**Figure 7.14 :** dLST map of Menderes.

Figure 7.15 : LST map of satellite image dated July 16, 2017 between 34 – 45 C°.

After the fire in the Menderes forests, especially the land surface temperature values in the burned area increased from 1 to 11 C ° compared to unburned areas. This situation can be clarified due to the decrease in albedo, which is the ratio of the amount of reflected radiation to the total radiation, in the burned area. The burned area will absorb the majority of solar energy due to low albedo. Therefore, the land surface temperature of the burned area is warmer than the unburned forest area.

7.5 Correlation Analysis

Correlation analysis is a statistical method that is utilised to search the strength of a association between two continuous variables that are numerically measured. The value of correlation coefficient range from -1 to +1. It is used to determine the possible connection of the variables. +1 means a positive perfect correlation, and -1 means a negative perfect correlation; on the other hand, if the correlation coefficient is 0, than there is no correlation between the variables.

Studies in the literature have shown a relationship between land surface temperature difference (dLST) and burning severity (dNBR) in burned forest areas. In this context, the high LST corresponds to the high burn severity and the low LST corresponds to the low burn severity [29].

In this study, a correlation analysis was performed between dLST and dNBR index values obtained from the pre-fire (30.06.2017) and post-fire (16.07.2017) Landsat 8 satellite images of the Menderes region. Correlation coefficient (R) between the two variables was found as R = 0.8138 (Figure 7.16).
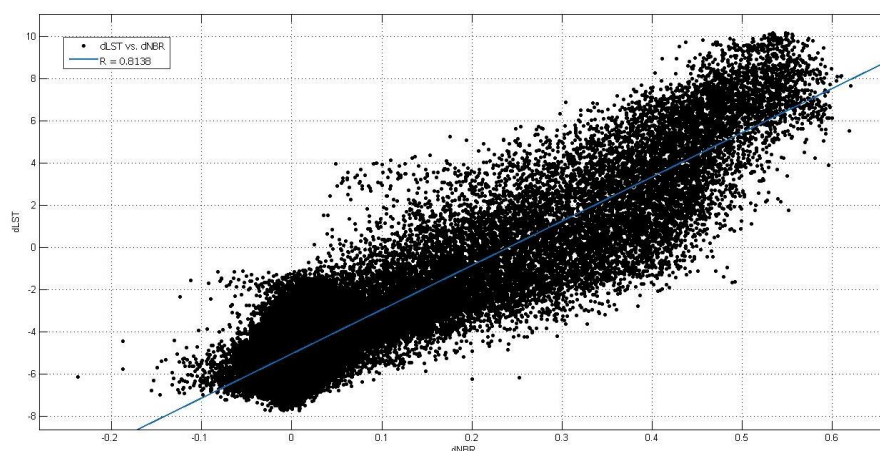

Figure 7.16 : Correlation analysis between dLST and dNBR (R = 0.8138).

Furthermore, to reveal the potential relationships of other spectral burn indexes (Burn Area Index, Normalized Burn Ratio – Thermal, and Mid-Infrared Burn Index) with dLST, the differences of pre-fire and post-fire Landsat 8 images of these indexes (dBAI, dNBRT, and dMIRBI) were determined. The correlation analysis of these indexes (dBAI, dNBRT, and dMIRBI) with dLST was performed.

As a result of the analysis, the correlation coefficient between dLST and dMIRBI was found as $R = -0.7520$, and the correlation coefficient of dLST and dNBRT was found as $R = 0.8567$, which means that these indexes are correlated with the land surface temperature difference. On the other hand, the correlation coefficient between dLST and dBAI was found as $R = 0$. Figure 7.17 shows the correlation analysis between dLST and dMIRBI, and Figure 7.18 shows the correlation analysis between dLST and dNBRT.
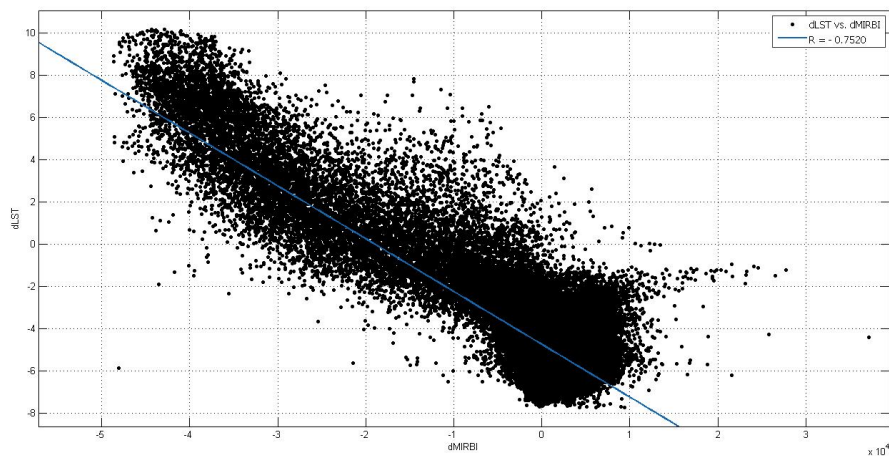

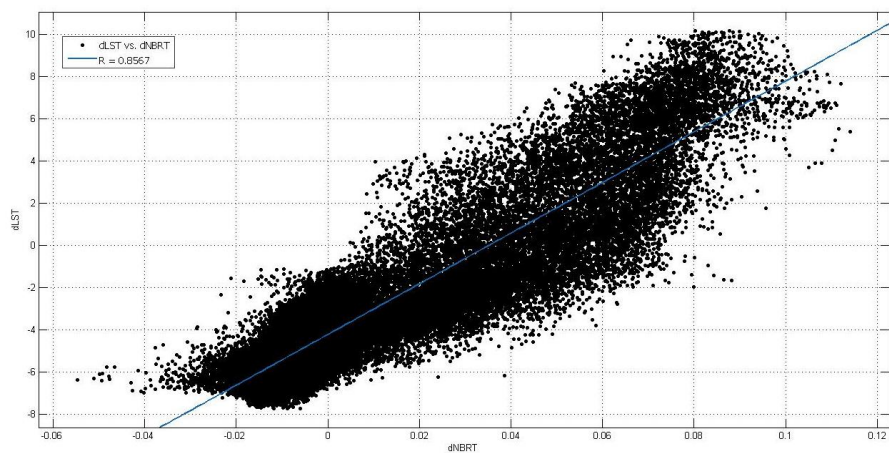**Figure 7.17 :** Correlation analysis between dLST and dMIRBI ($R = -0.7520$).

Figure 7.18 : Correlation analysis between dLST and dNBRT ($R = 0.8567$).

7.6 Image Classification

As mentioned earlier, image classification is one of the fundamental image processing methods that is applied to remotely sensed data to categorize the image pixels to the land cover classes. In this study, unsupervised and supervised classification processes are done for both Sentinel 2 and Landsat 8 images. After this processes, thematic maps were generated and the areal extent of the fire area was calculated.

7.6.1 Unsupervised classification

ISODATA classification algorithm with 9 classes was performed for the Landsat 8 satellite image dated July 16, 2017 with 30 m spatial resolution, and the Sentinel 2 satellites images dated July 22, 2017 with 20 m and 10 m spatial resolution. After the classification process, all the calculated areal extent of the burned area of these satellite images having different spatial resolutions (10 m and 20 m Sentienl 2, and 30 m Landsat 8) were compared to each other and also with the original GIS data created by the Izmir Forestry Chief Directorate during a field work.

First of all, post-fire Landsat 8 satellite image (16.07.2017) was classified with the ISODATA algorithm. The major 6 classes generated are burned forest area, lake, bare soil, forest, agriculture, and settlement area.

Afterwards, post-fire Sentinel 2 satellite images (22.07.2017) with 20 m and 10 m spatial resolution were classified with the ISODATA method like the Landsat 8 image. The major 6 classes are same with Landsat 8 thematic map.

As stated by Izmir Chief Directorate, the exact burned forest area of Menderes is 986 ha, which is calculated after a field work. The total forest area within the borders of the Menderes Forestry Chief Directorate is 24957 ha. This states that the fire destroyed 4% of the total forest area. The burned forest area was found as 972,9 ha, 938,61 ha, and 926,91 ha for the 10 m Sentinel, 20 m Sentinel, and 30 m Landsat 8 satellite images respectively (Figure 7.19).
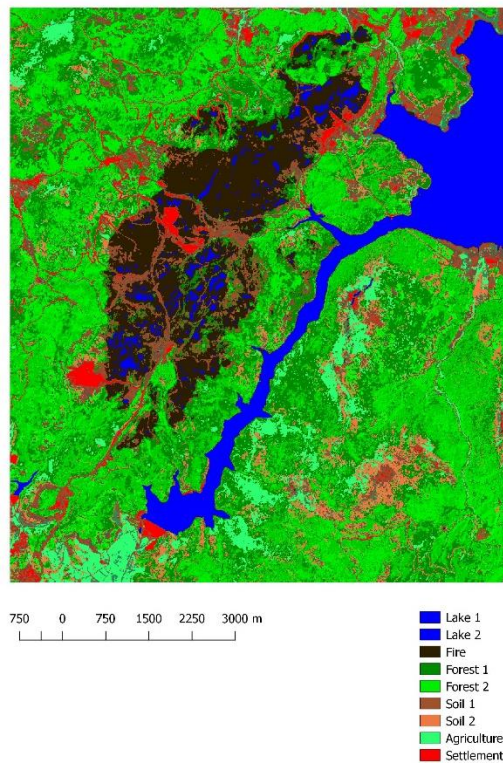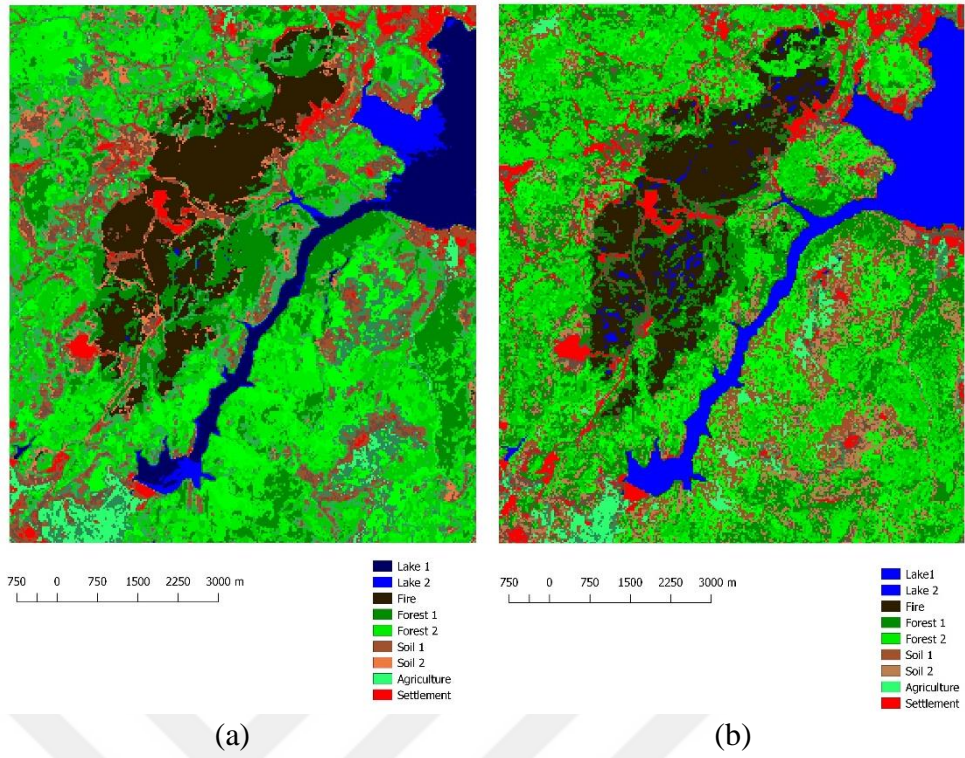
Figure 7.19 : ISODATA classification. (a) Landsat 8 (30 m) (b) Sentinel 2 (20 m) Sentinel 2 (10 m)

It is seen that mine areas are mixed and classified as settlement area on three thematic maps. Furthermore, burned fores area classes on both Sentinel 2 satellite images are mixed with the lake class.

The class statistics of the burned forest area are calculated and shown graphically on the Figure 7.20.
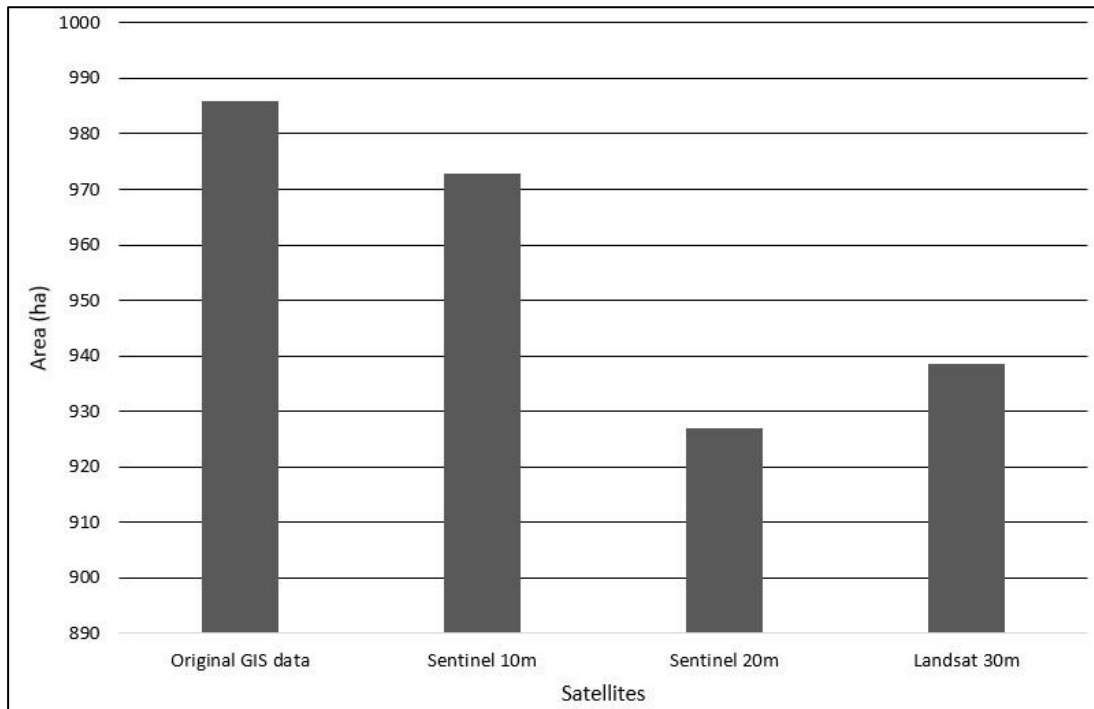

Figure 7.20 : The areal extents of the burned forest area mapped by ISODATA classification.

7.6.2 Supervised classification

In a similar manner to unsupervised classification, supervised classification was performed using same bands for Landsat 8 and Sentinel 2 data sets. The Maximum Likelihood and Support Vector Machine classification algorithms were applied to these satellite images as supervised classification method.

Regions of Interests (ROIs) are used to define the training areas carefully. The 7 training areas which are selected on the satellite images are burned forest area, lake, bare soil, forest, agriculture, settlement, and mine area (Figure 7.20). While region of interests (ROIs) are being selected, forest management plan and the GIS data supplied by the Izmir Forestry Chief Directorate are used as ground truth data.

Firstly, the ROIs were selected to train the post-fire Landsat 8 satellite image as shown on the Figure 7.21.
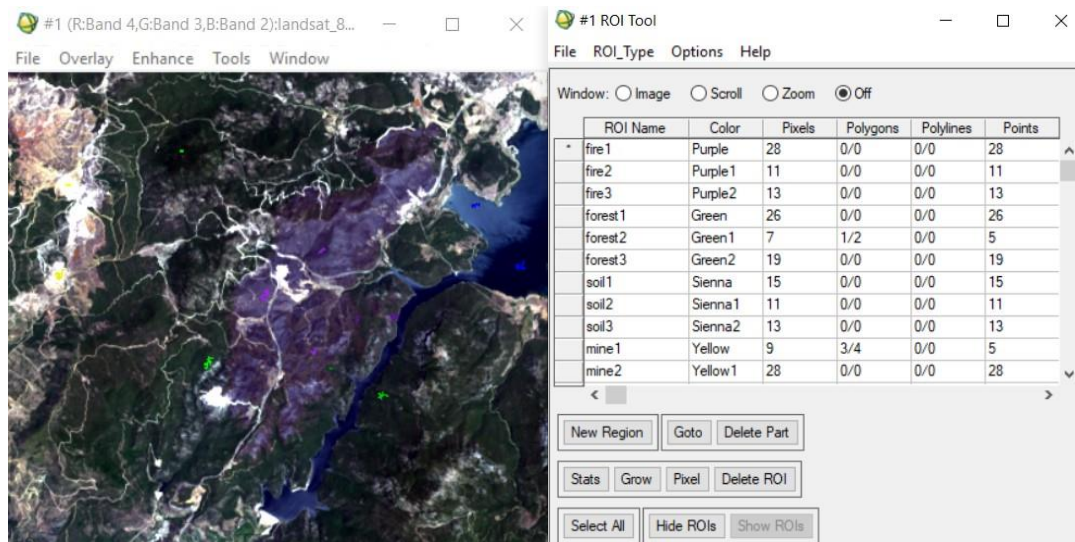
Figure 7.21 : Selected ROIs on the Landsat 8 satellite image.

Afterwards, the Maximum Likelihood classification algorithm was applied on July 16, 2017 dated post-fire Landsat 8 satellite image. The same process were performed on Sentinel 20 m and 10 m post-fire images dated July 22, 2017 (Figure 7.22).

Burned forest areas were determined as 962.37 ha, 963,36 ha, and 911,34 ha for 10 m Sentinel, 20 m Sentinel, and 30 m Landsat 8 satellite images respectively.

The efficiencies of Sentinel 2A and Landsat 8 satellites were compared with Overall accuracies, and computed as 96.43 %, 82.22 %, and 80.30 % for Sentinel (10 m), Sentinel (20 m), and Landsat (30 m) forest fire thematic maps respectively, after the supervised classification process (Table 7.3).

Table 7.3 : Overall accuracies of the Maximum Likelihood classification results.

Image	Overall Accuracy (%)
Sentinel (10 m)	96.43
Sentinel (20 m)	82.22
Landsat 8 (30 m)	80.30

According to the accuracy results, Sentinel 2 with 10 m spatial resolution image classification gave the best result regard to the higher spatial resolution.
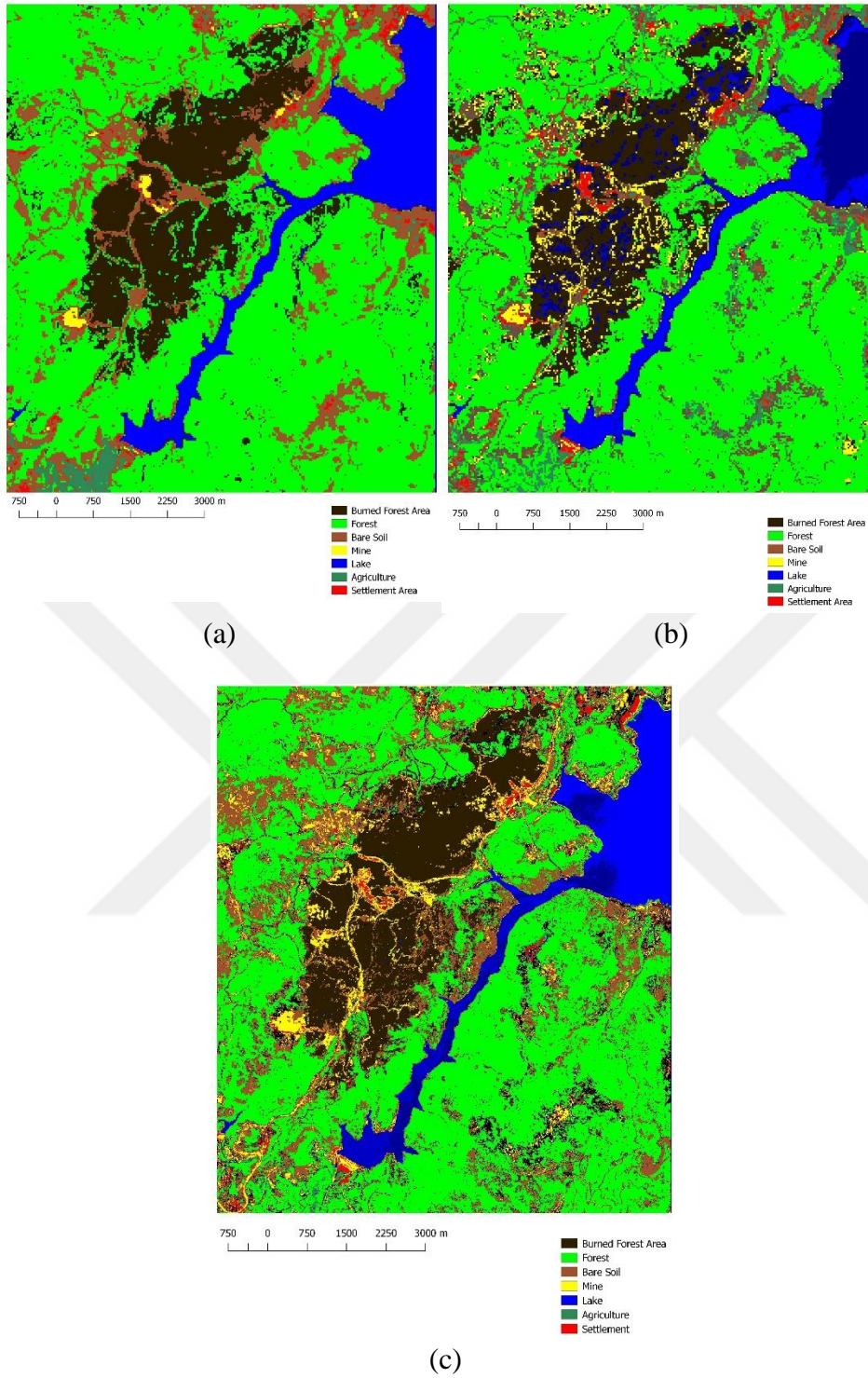
Figure 7.22 : Maximum Likelihood classification. (a) Landsat 8 (30 m) (b) Sentinel 2 (20 m) Sentinel 2 (10 m)

The class statistics of the burned forest area are calculated and shown graphically on the Figure 7.23.
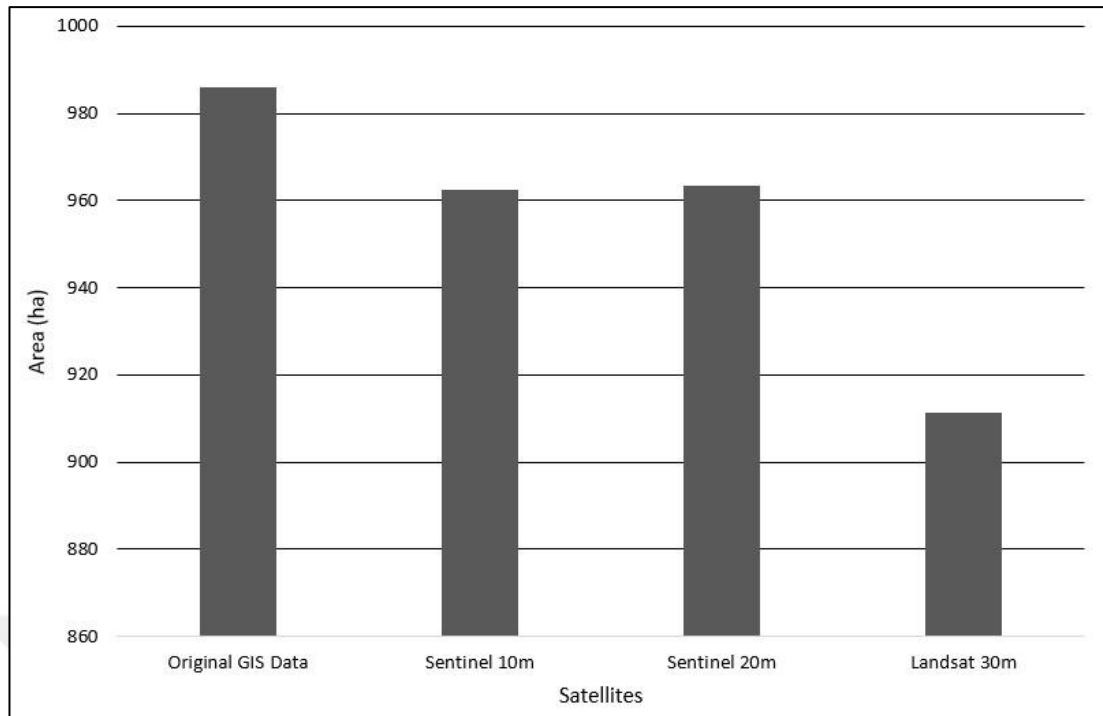
Figure 7.23 : The areal extents of the burned forest area mapped by Maximum Likelihood classification.

Support Vector Machine classification algorithm was also performed as a supervised classification method to all three images for identifying the areal extent of burned forest area (Figure 7.24). As same as Maximum Likelihood classification, 7 training areas were selected on the satellite images as burned forest area, lake, bare soil, forest, agriculture, settlement, and mine area. After the class statistics analysis burned forest areas were computed as 991,35 ha, 994,65 ha, and 997,11 ha for 10 m Sentinel, 20 m Sentinel, and 30 m Landsat 8 satellite images respectively. Furthermore, the overall accuracies of the classification results were found as 99.56 %, 97.86 %, and 97.52 % for 10 m Sentinel, 20 m Sentinel, and 30 m Landsat 8 images respectively (Table 7.4).

Table 7.4 : Overall accuracies of the Support Vector Machine classification results.

Image	Overall Accuracy (%)
Sentinel (10 m)	99.56
Sentinel (20 m)	97.86
Landsat 8 (30 m)	97.52

Similarly, Sentinel 2 (10 m) image classification gave the best result regard to the higher spatial resolution.
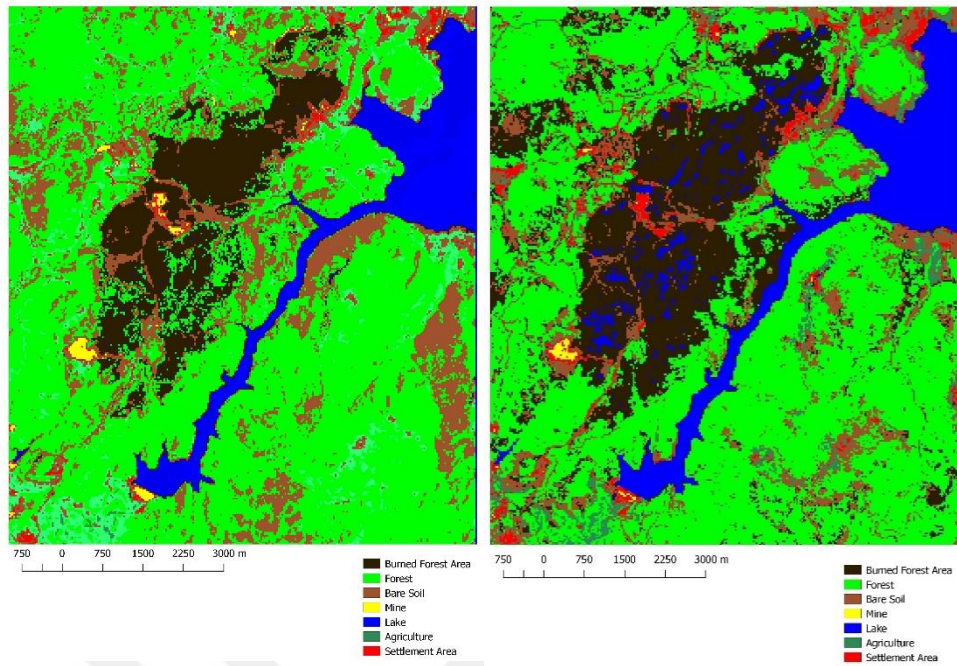
(a)

(b)
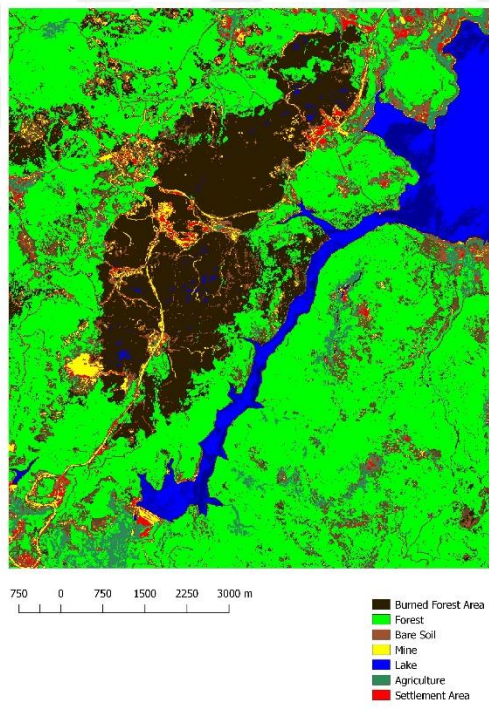
(c)

Figure 7.24 : Support Vector Machine classification. (a) Landsat 8 (30 m) (b)
Sentinel 2 (20 m) (c) Sentinel 2 (10 m)

The class statistics of the burned forest area are calculated and shown graphically on
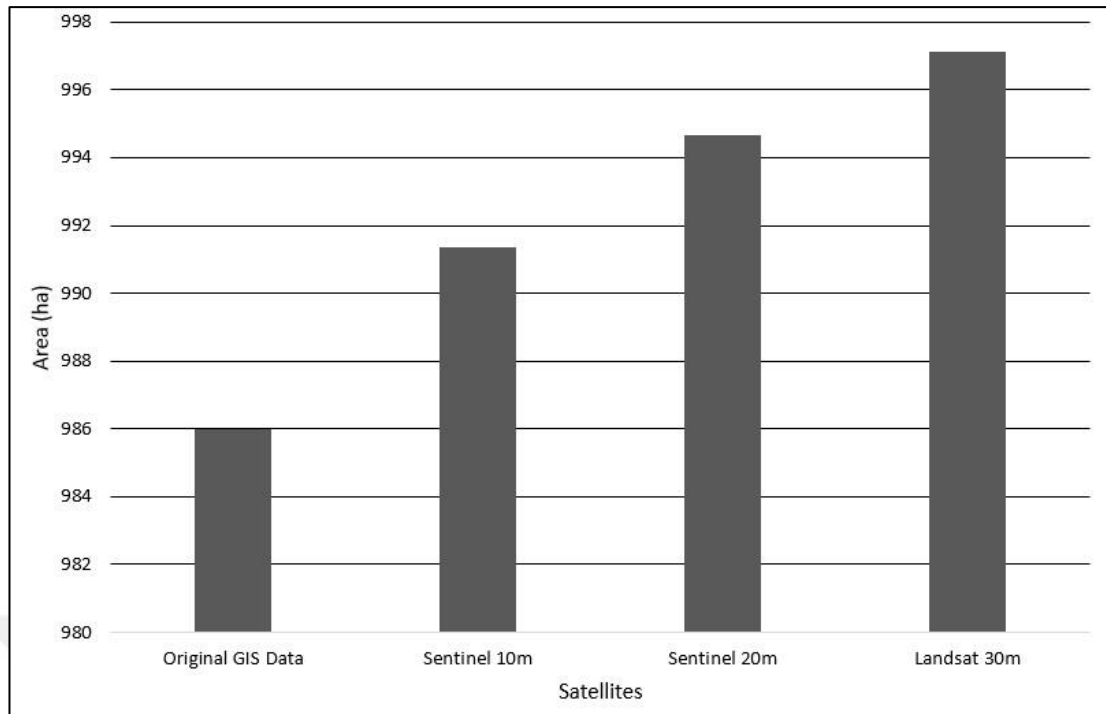the Figure 7.25.

Figure 7.25 : The burned forest area mapped by Support Vector Machine classification.

7.7 GIS Integration

Finally, the Menderes forest fire was analyzed by using the GIS data obtained after a field study conducted by the Izmir Foresrty Chief Directorate. Taking advantage of the ground truth, all potential factors that affecting the fire have been revealed.

The litarature review have been shown that some topographical parameters such as vegetation type, slope, and canopy are the fundamental parameters which affecting a forest fire. It is revealed that forest fires occuring mainly in Black Pine (*Pinus nigra*) and Calabrian Pine (*Pinus brutia*) forests due to their extremely burnability in Turkey. As previously mentioned, the burned forest area in Menderes is covered only with Calabrian Pine forest species [44].

Because of the high canopy density (71 – 100 %) which leads to natural branch pruning and debris of cuts, the quantity of dead plant is increasing on the forest area; therefore, it is very easy to spread out for the fire. Moreover, it is also monitored from previous forest fires in Turkey that slope with a range of 8 to 35 % may cause broad forest fires.

In this context, GIS maps in a 1 : 30 000 scale that demontrates the canopy density and also the slope of the Menderes forest area were produced (Figure 7.26 a and b).

Afterwards, the relationship of the canopy density and slope were revealed, and also mapped (Figure 7.26 c).

As a result, it is proven that areas having canopy density between 71 – 100 % and slope from 29 to 41% were mostly burned in the Menderes region.

Furthermore, the relationship of canopy density, slope and burn severity were also determined, and mapped (Figure 7.26 d).

According to the results canopy density between 71 – 100 % and slope from 29 to 41% were mainly determined as low burn severity. However, it was observed that the burn severity was increased (moderate low and high severity) with the increase of slope (42 – 54%).
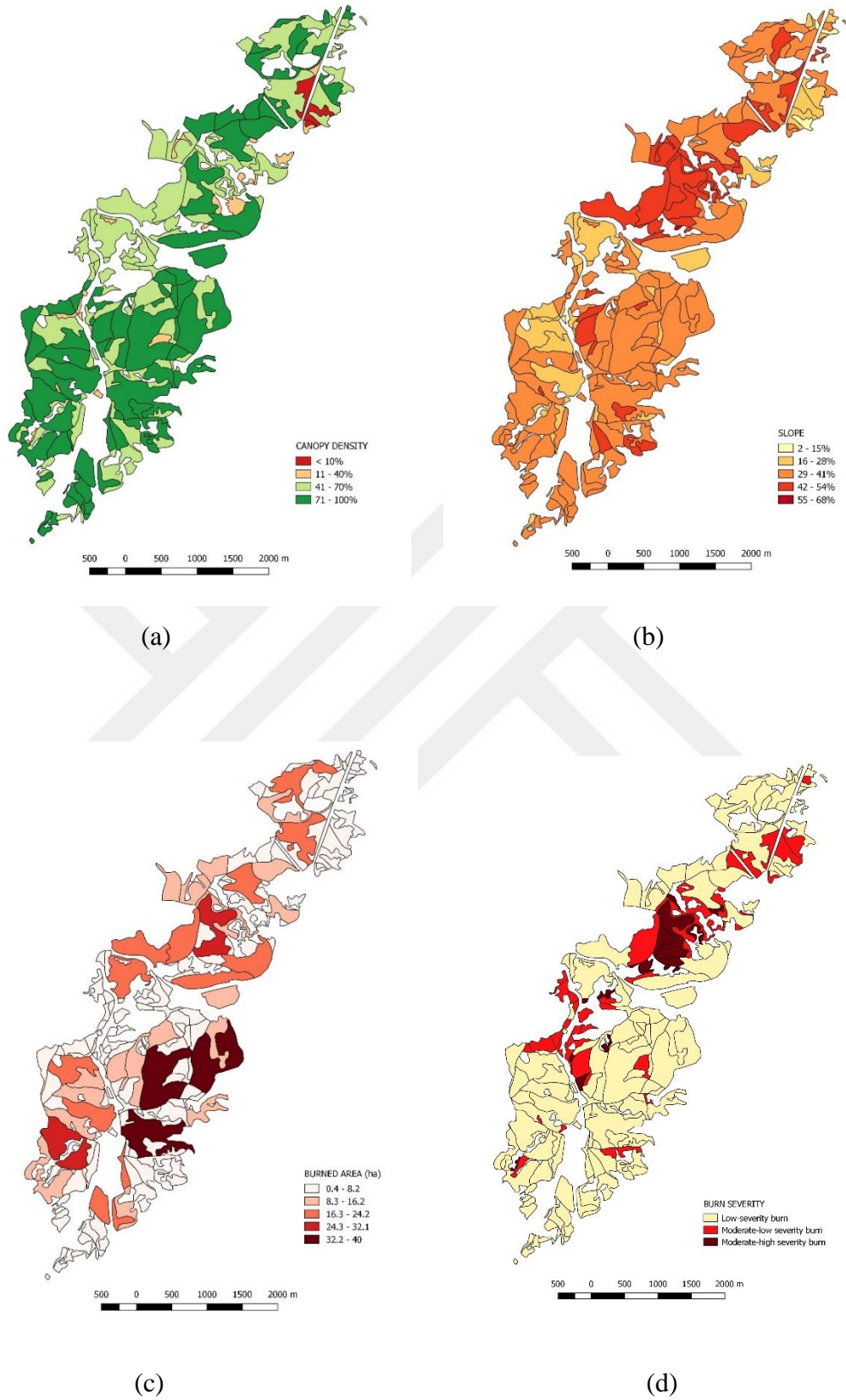
Figure 7.26 : GIS maps of Menderes area. (a) Slope (b) Canopy Density (c) The bilateral effect of canopy density and slope on burned forest areas (d) The bilateral effect of canopy density and slope on burn severity.

8. CONCLUSION

In the 21st century, our planet is facing problems such as population growth, reduction of natural resources, and natural disasters. Forest fires are one of the siginificant problems as natural disasters. It is defined as an ecological disaster caused by human or natural causes. Furthermore, forest fires, which affect the terrestrial ecosystem and the atmospheric system on a large scale, cause deforestation and greenhouse gas emissions, and also affect the human welfare greatly. In the last two decades, 33508 hectares of forest area were destroyed by forest fires just in Turkey. The use of science and technology, especially remote sensing, is critical to find rational solutions to these problems.

In this study, remote sensing techniques such as spectral burn indexes (Burn Area Index (BAI), Normalized Burn Ratio (NBR) and Normalized Burn Ratio – Thermal (NBRT) and Mid-Infrared Burn Index (MIRBI)), burn severity (dNBR), land surface temperature determination, and classification, and the use of GIS were utilised to observe, analyse, and map the environmetal changes of a forest fire occured in Menderes, Izmir in 2017.

First of all, the spectral burn indexes like BAI, NBR, NBRT, and MIRBI were applied on the post-fire (16.07.17) Landsat 8 satellite image to isolate and analyse the burned forest area. The NBR and NBRT indexes were very succesful to distinguish the burned forest area from unburned areas like healthy forest, mine, and settlement area. On the other hand, it is observed that the BAI and MIRBI indexes could not completely separated the burned forest area from unburned areas, and they are mixed with other land covers especially with water bodies.

Afterwards, the dNBR index which removes the post-fire NBR data set from pre-fire NBR dataset was used to estimate the burn severity. For this purpose, Landsat 8 satellite images dated July 16, 2017 and June 30, 2017 were used as post-fire and pre-fire NBR datasets respectively. The same process was performed on the post-fire

71

Landsat 8 image dated July 3, 2018 to monitor the vegetation survival and mortality after one year later of the fire as the dNBR index shows also the vegetation regrowth. As a result, no vegetation regrowth was observed in the forest area after one year, and the effects of the fire is still identical.

Land Surface Temperature (LST) was also determined by the use of land surface temperature algorithm to monitor the changes of LST (dLST) in the Menderes region from pre-fire (30.06.2017) and post-fire (16.07.2017) Landsat 8 images. Accordingly, it was observed that the LST of the burned forest area was increased from 1 to 11 C° compared to unburned areas. The reason for the LST increase in burned areas is thought as the decrease of albedo.

A correlation analysis was also performed on dLST and dNBR (burn severity) to monitor the possible relationship on these two variables. Eventually, a high correlation (R = 0.8138) was observed between the dNBR and the dLST. This situation means that the high LST corresponds to the high burn severity and the low LST corresponds to the low burn severity. In addition, correlation analysis of dBAI, dMIRBI and dNBRT, obtained from other spectral burn indexes, with the surface temperature difference (dLST) data were performed; moreover, dMIRBI and dNBRT indexes were found to be related to dLST (R = -0.7520 and R = 0.8567, repectively). On the other hand, there is no relationship between dBAI and dLST (R = 0).

Unsupervised and supervised classification processes were done for post-fire Sentinel 2 (22.07.2017) images with 10 m and 20 m spatial resolution, and Landsat 8 image (16.07.2017) with 30 m spatial resolution to compute the areal extent of burned forest area, and also to compare the efficiency of overall accuracies of supervised classification results of satellite images with different spatial resoultions. After applying the ISODATA classification algorithm as unsupervised classification method on three mentioned images, the area extent of burned areas was found as 972,9 ha, 938,61 ha, and 926,91 ha for the 10 m Sentinel, 20 m Sentinel, and 30 m Landsat 8 satellite images respectively. As supervised classification method Maximum Likelihood and Support Vector Machine classification algorithm were performed on post-fire satellite images. Consequently, from the Maximum Likelihood method the best result was determined by 10 m Sentinel as 962.37 ha with a 96.43% overall accuracy; on the other hand, the worst result was determined by 30 m Landsat 8 satellite image as 911.34 ha with a 80.30% overall accuracy. From the Support Vector

Machine algorithm the best result was determined by 10 m Sentinel as 991.35 ha with a 99.56% overall accuracy; however, the worst result was determined by 30 m Landsat 8 satellite image as 997.11 ha with a 97.52% overall accuracy.

Finally, a GIS data was integrated with the remote sensing images, and a slope and canopy density map were generated, and their relationship with the burned forest area and burn severity were revealed. It was observed that slope from 29 to 41%, and the canopy density between 71 and 100 % were highly related to the burned forest area. Moreover, according to the results slope from 29 to 41%, and the canopy density between 71 and 100 % were mostly determined as low burn severity.

As a result, it is crucial to develop and use remote sensing and GIS techniques to monitor forest fires that cause deforestation in the area and also greenhouse gas emissions for the future of the planet Earth. In this context, the advanced forest fire monitoring systems including space and digital image processing technologies must be established to ensure the sustainability of forest ecosystems.

REFERENCES

[1] **Chuvieco, E.** (2016). *Fundamentals of Satellite Remote Sensing: An Environmental Approach*, NY: CRC Press.

[2] **Campbell, J. B. and Wynne, L.** (2011). *Introduction to Remote Sensing*, NY: The Guilford Press.

[3] **Weng, Q.** (2010) *Remote Sensing and GIS Integration: Theories, Methods, and Applications*. NY: The McGraw – Hill Companies.

[4] **Chuvieco, E. and Congalton, R.G**. (1989). Application of remote sensing and geographic information systems to forest fire hazard mapping. *Remote Sensing of Environment*, **29**, 147-159.

[5] **Sonti, S.H.** (2015). *Application of Geographic Information System (GIS) in Forest Management*. Retrieved September 5, 2018, from https://www.omicsonline.org/open-access/application-of-geographic-information-system-gis-in-forest-management-2167-0587-1000145.php?aid=64974

[6] **Rees, W.G.** (2012). *Physical Principles of Remote Sensing*, Cambridge: Cambridge University Press

[7] **Sunar, F., Çoşkun, Ö., and Osmanoğlu, B.** (2011). *Uzaktan Algılama [Remote Sensing]*, Eskişehir: Anadolu Üniversitesi.

[8] **Url-1** <https://byjus.com/physics/electromagnetic-radiation/>, date retrieved 06.09.2018.

[9] **Novgorodova, G.** (2015). *Concerning the light: remote sensing basics*. Retrieved September 10, 2018, from http://www.50northspatial.org/concerning-the-light/

[10] **Avery, T.E. and Berlin, G.L.** (1992). *Fundamentals of remote sensing and airphoto interpretation,* USA: Macmillan.

[11] **Vegetation Spectral Reflectance Curves.** (n.d.). Retrieved September 11, 2018, from http://gsp.humboldt.edu/OLM/Courses/GSP_216_Online/lesson2-1/vegetation.html

[12] **Malinowski, R., Groom, G., Schwanghart, W. and Heckrath, G.** (2015). Detection and delineation of localized flooding from worldview-2 multispectral data. *Remote Sens.*, **7**, 14853-14875.

[13] **Weng, Q.** (2012). *An Introduction to Contemporary Remote Sensing*. China: The McGraw – Hill Companies.

[14] **National Aeronautics and Space Administration.** (2015). *Landsat*. Retrieved from

https://www.nasa.gov/mission_pages/landsat/overview/index.html

[15] **National Aeronautics and Space Administration.** (n.d.). *History*. Retrieved from https://landsat.gsfc.nasa.gov/about/history/

[16] **National Aeronautics and Space Administration.** (2017). *Landsat 8*. Retrieved from https://nssdc.gsfc.nasa.gov/nmc/spacecraftDisplay.do?id=2013-008A

[17] **National Aeronautics and Space Administration.** (2018). *What are the band designations for the Landsat satellites?*. Retrieved from https://landsat.usgs.gov/what-are-band-designations-landsat-satellites

[18] **U.S. Geological Survey.** (2016). *Landsat 8 (L8) Data Users Handbook*, Retrieved from https://landsat.usgs.gov/sites/default/files/documents/Landsat8DataUsersHandbook.pdf

[19] **Url-2** <http://ec.europa.eu/growth/sectors/space/copernicus_en>, date retrieved 10.10.2018.

[20] **Url-3** <http://www.copernicus.eu/main/sentinels>, date retrieved 10.10.2018.

[21] **European Space Agency.** (n.d.). *MultiSpectral Instrument (MSI)*. Retrieved from https://sentinels.copernicus.eu/web/sentinel/missions/sentinel-2/instrument-payload

[22] **Url-3** <https://www.satimagingcorp.com/satellite-sensors/other-satellite-sensors/sentinel-2a/>, date retrieved 10.10.2018.

[23] **Longley, P.A., Goodchild, M.F., Maguire, D.J. and Rhind D.W.** (2005). *Geographical Information Systems and Science*. England: John Wiley & Sons.

[24] **Reddy, M.A.** (2008). *Remote Sensing and Geographical Information Systems*. India: BSP.

[25] **Url-4** <http://www.geologiveneto.it/evento/settimana-della-consapevolezza-geografica/>, date retrieved 11.10.2018.

[26] **Valero, M., Rios, O., Mata, C., Pastor, E. and Planas, E.** (2018). GIS-based integration of spatial and remote sensing data for wildfire monitoring. *International Symposium on Remote Sensing*, Alpensia Convention Center, Korea, 9-11 May.

[27] **Adab, H., Kanniah, K.D. and Solaimani, K.** (2013). Modeling forest fire risk in the northeast of Iran using remote sensing and GIS techniques. *Nat. Hazards*, **65**, 1723-1743.

[28] **Jaiswal, R.K., Mukherjee, S., Raju, K.D. and Saxena, R.** (2002). Forest fire risk zone mapping from satellite imagery and GIS. *International Journal of Applied Earth Observation and Geoinformation,* **4**, 1-10.

[29] **Vlassova, L., Perez-Cabello, F., Mimbrero, M.R., Llovera, R.M. and Garca-Martin, A.** (2014). Analysis of the relationship between land surface temperature and wildfire severity in a series of landsat images. *Remote Sens.*, **6**, 6136-6162.

[30] **Quintano, C., Fernandez-Manso, A., Calvo, L., Marcos, E. and Valbuena, L.** (2015). Land surface temperature as potential indicator of burn severity in forest mediterranean ecosystems. *International Journal of Applied Earth Observation and Geoinformation*, **35**, 1-12.

[31] **Guangmeng, G. and Mei, Z.** (2004). Using MODIS land surface temperature to evaluate forest fire risk of northeast China. *IEEE Geoscience and Remote Sensing Letters*, **1**, 98-100.

[32] **Anitha, S., Sounjanya, S. and Rajkumar, G.B.** (2013). An approach for identifying the forest fire using land surface ımagery by locating the abnormal temperature distribution. I*OSR Journal of Computer Engineering*, **14**, 6-12.

[33] **Norton, J.** (2008). *The Use of Remote Sensing Indices to Determine Wildland Burn Severity in Semiarid Sagebrush Steppe Rangelands Using Landsat ETM + and SPOT 5*, Retrieved from https://pdfs.semanticscholar.org/4233/597fb51c5a29b4c282381081fa0 a223a7341.pdf?_ga=2.222787999.589094   426.1533223500-1622772386.1533223500

[34] **Sunar, F. and Özkan, C.** (2001). Forest firere analysis with remote sensing data. *International Journal of Remote Sensing*, **22**, 2265-2277.

[35] **Sunar, F., Özkan, C., Ok, A.Ö., Osmanoğlu, B., Avcı, Z.D.U. and Berberoğlu, S.** (2017). *Digital Image Processing [Dijital Görüntü İşleme]*, Eskişehir: Anadolu Üniversitesi.

[36] **Jahne, B.** (2002). *Digital Image Processing*, Berlin: Springer.

[37] **Remote Sensing Systems.** (n.d.) Retrieved from http://gis.humboldt.edu/club/Images/Documents/lecture7.pdf

[38] **Philpot, W.** (n.d.). *Geometric Correction*. Retrieved from http://ceeserver.cee.cornell.edu/wdp2/cee6150/Lectures/DIP06_GeoCorrect_Sp14.pdf

[39] **Key, C.H., and Benson, N.C.** (2005). *Landscape assessment (LA) sampling and analysis methods. In book: FIREMON: Fire Effects Monitoring and Inventory System. Edition: Gen. Tech. Rep. RMRS-GTR-164. Publisher: USDA Forest Service, Rocky Mountain Research Station, Ogden, UT.* (Editors: D.C. Lutes, R.E. Keane, J.F. Caratti, C.H. Key, N.C. Benson, S. Sutherland, L.J. Gangi). Retrieved from https://www.fs.fed.us/postfirevegcondition/documents/publications/FIREMON_LandscapeAssessment.pdf

[40] **Holden, Z.A., Smith, A.M.S., Morgan, P., Rollins, M.G., and Gessler, P.E.** (2005). Evaluation of novel thermally enhanced spectral indices for mapping fire perimeters and comparisons with fire atlas data. *International Journal of Remote Sensing*, *26*, 4801-4808. https://doi.org/10.1080/01431160500239008

[41] **Schepers, L., Haest, B., Veraverbeke, S., Spanhove, T., Borre, J.V., and Goossens, R.** (2014). Burned area detection and burn severity assessment of a heathland fire in belgium using airborne imaging spectroscopy (apex). *Remote Sensing*, *6*, 1803-1826. https://doi.org/10.3390/rs6031803

[42] **Giannini, M.B., Belfiore, O.R., Parente, C. and Santamaria, R.** (2015). Land Surface Temperature from Landsat 5 TM images: comparison of different methods using airborne thermal data, *Journal of Engineering Science and Technology Review*, *8*, 83-90.

[43] **Url-5** <http://shodhganga.inflibnet.ac.in/bitstream/10603/24460/10/10_chapter5.pdf>, date retrieved 25.10.2018.

[44] **Akkaş, M.E., Bucak, C., Boza, Z., Eronat, H., Bekereci, A., Erkan, A., and Cebeci, C.** (2006). *Büyük orman yangınlarının meteorolojik verilerin ışığında incelenmesi [The investigation of the great wild fires based on meteorological data].* Retrieved from https://www.cem.gov.tr/erozyon/files/erozyon/yardop.../yangin_ meteoroloji_iliskisi_2.doc

[45] **Url-6** <http://gsp.humboldt.edu/OLM/Courses/GSP_216_Online/lesson2-1/reflectance.html>, date retrieved 01.11.2018.

[46] **Mesev, V.** (2007). *Integration of GIS and Remote Sensing,* England: John Wiley & Sons.

CURRICULUM VITAE

Name Surname	**:** Emre Çolak
Place and Date of Birth	**:** Bad Kreuznach, Germany / 06.01.1994
E-Mail	**:** colakem@itu.edu.tr

EDUCATION **:**

- **B.Sc.** **:** 2017, Istanbul Technical University, Faculty of Civil Engineering, Department of Geomatics Engineering

PROFESSIONAL EXPERIENCE AND REWARDS:

- 2017 Second degree graduation in BSc at ISTANBUL Technical University
- 2016 GISLAB, Göktürk Satellite Program Operator Translation (English - Turkish)
- 2016 IMAJ Surveying, Mining and Computer Company (ISTANBUL)
- 2015 ISTANBUL Technical University Research and Application Center for Satellite Communications and Remote Sensing (Internship)
- 2012 First degree graduation in High School (ISTANBUL)

PUBLICATIONS, PRESENTATIONS AND PATENTS ON THE THESIS:

- **Çolak, E. and Sunar F.** 2018. Remote Sensing & GIS Integration For Monitoring The Areas Affected By Forest Fires: A Case Study In Izmir, Turkey. GI4DM, March 18-21, 2018 Istanbul, Turkey. (Poster Instance)

- **Çolak, E. and Sunar F.** 2018. Use Of Surface Temperature And Spectral Burn Indexes In Forest Fire Analysis. UZAL-CBS. September 18-21, 2018 Eskişehir, Turkey. (Presentation Instance)

OTHER PUBLICATIONS, PRESENTATIONS AND PATENTS:

- **Esenbuğa, O. G., Akoğuz, A., Çolak, E., Varol, B. and Erol, B.** 2016. Comparison Of Principal Geodetic Distance Calculation Methods For Automated Province Assignment In Turkey. *SGEM Conference Proceedings*, 2(2), 141-148. (Article Instance)
- **Tunç, A., Şenel, M. and Çolak, E.** 2017. The Impact of Syrian Immigrants on Istanbul Tourism Flow. MESAEP. October 4-6, 2017 Rome, Italy. (Presentation Instance)
- **Şenel, M. and Çolak, E.** 2016. Creating a City Information System for the Detemination of Bookstores With Literary Journals in Istanbul. [İstanbul'da Edebiyat Dergilerini Bulunduran Sahaf ve Kitapçıların Tespiti için Kent Bilgi Sisteminin Oluşturulması]. WORLD GIS DAY. November 24-25 Istanbul, Turkey. (Poster Instance)